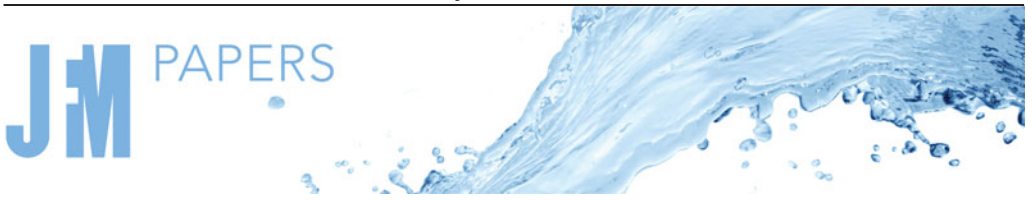
J. Fluid Mech. (2021), *vol*. 923, A19, doi:10.1017/jfm.2021.580



Dynamics of a trefoil knotted vortex

Jie Yao[1], **Yue Yang**[2] **and Fazle Hussain**[1],†

[1]Department of Mechanical Engineering, Texas Tech University, Lubbock, TX 79409, USA

[2]State Key Laboratory for Turbulence and Complex Systems, College of Engineering, Peking University, Beijing 100871, PR China

(Received 3 November 2020; revised 21 June 2021; accepted 22 June 2021)

A slender trefoil knotted vortex is studied using direct numerical simulation of the Navier–Stokes equations for vortex Reynolds numbers ($Re \equiv \Gamma/\nu$, circulation/viscosity) up to 12 000. For initially zero twist ($T_{w,0} = 0$), neither the writhe W_r nor the global helicity H is conserved. Initially W_r slowly decreases, then suddenly drops during reconnection and becomes almost constant thence; its evolution is almost Re independent. Before reconnection, H also gradually decreases but sharply increases during reconnection. The evolution of H after reconnection strongly depends on Re. While steadily decreasing at low Re, H significantly increases before eventually decaying at high Re. Flow visualization, helicity decomposition and helical wave decomposition reveal that significant amounts of positive and negative twist helicities are simultaneously generated before and during reconnection. Also, the small leading and large trailing rings resulting from asymmetric reconnection have respectively negative and positive twists, which then decay differently due to different initial values, geometries and mutual induction. In particular, at high Re, the twist in the small ring, under stretching by the large trailing ring, decays much faster and even switches sign to become positive by the writhe-to-twist conversion – the main reason for the 'transient growth' of H. Simulations with non-zero initial twists ($T_{w,0} = 7.48$ and 22.48) reveal that the overall dynamics is similar to the $T_{w,0} = 0$ case. Hence, the evolution of the trefoil knotted vortex is mainly governed by W_r, not T_w, although the latter is found to play an essential role in enstrophy growth as well as energy cascade.

Key words: vortex dynamics, vortex interactions

1. Introduction

As a fundamental topology transforming event, reconnection has been extensively studied over recent decades, both in classical (Ashurst & Meiron 1987; Melander & Hussain 1988; Kida, Takaoka & Hussain 1991; Kida & Takaoka 1994; Hussain & Duraisamy

† Email address for correspondence: fazle.hussain@ttu.edu

© The Author(s), 2021. Published by Cambridge University Press

https://doi.org/10.1017/jfm.2021.580 Published online by Cambridge University Press

2011) and in quantum (Koplik & Levine 1993; Bewley *et al.* 2008; Zuccher *et al.* 2012; Fonda, Sreenivasan & Lathrop 2019) fluids, as well as in many other subjects, such as plasmas (Priest & Forbes 2000) and macromolecules (Vazquez & Sumners 2004). It plays a significant role in numerous turbulence phenomena, such as energy cascade (Kivotides *et al.* 2001; Yao & Hussain 2020*b*), flow transition (Zhao, Yang & Chen 2016), fine-scale mixing (Hussain 1986) and noise generation (Daryan, Hussain & Hickey 2020).

Prior studies on vortex reconnection have mainly focused on relatively simple configurations: vortex rings (Kida *et al.* 1991; McKeown *et al.* 2018), orthogonal vortices or colliding dipoles (Melander & Zabusky 1988; Boratav, Pelz & Zabusky 1992; Orlandi, Pirozzoli & Carnevale 2012; Jaque & Fuentes 2017), and anti-parallel vortices with a sinusoidal displacement (Pumir & Kerr 1987; Melander & Hussain 1988). Note that reconnection physics of two vortices should be independent of the initial spatial configuration, as two vortex filaments with arbitrary orientations tend to become anti-parallel by mutual induction as they approach each other (Siggia 1985). In general, there are three typical stages of viscous vortex reconnection: inviscid advection, bridging and threading (Melander & Hussain 1988). During reconnection, extremely small scales can be generated due to vortex stretching; as a result, a sufficiently high resolution is required to capture these structures. Hence, previous direct numerical simulation (DNS) studies of reconnection in classical fluids mainly focused on small-scale problems, such as those with a large core size compared with the domain size and at low to moderate Reynolds numbers (Pumir & Kerr 1987; Melander & Hussain 1988; Shelley, Meiron & Orszag 1993; Chatelain, Kivotides & Leonard 2003; Kerr 2013). With the rapid development of supercomputers these days, DNS of considerably large-scale problems is becoming feasible (Lee & Moser 2015; Iyer, Sreenivasan & Yeung 2017). Recent work on vortex reconnection at high Reynolds numbers has revealed more rich phenomena, such as reconnection cascade, where the threads undergo successive reconnections to form secondary vortex rings and a turbulence avalanche (Yao & Hussain 2020*b*).

Another type of configuration that has a particular interest is the knotted vortex tube. It has a close relationship to an important quantity: helicity H, which is defined as $H = \int_V h \,\mathrm{d}V$, with V the entire flow domain and $h = \boldsymbol{u} \cdot \boldsymbol{\omega}$ being the helicity density ($\boldsymbol{u}$ and $\boldsymbol{\omega}$ are the velocity and vorticity, respectively). Helicity measures the degree to which vortex lines embedded in a fluid system wind around each other (Moffatt 1969; Scheeler *et al.* 2017). Similar to energy, helicity is also conserved in ideal fluids and is expected to have a strong influence on the flow evolution. For finite thickness vortex tubes, the helicity can be further geometrically expressed as (Moffatt & Ricca 1992; Scheeler *et al.* 2014)

$$H = \sum_{i \neq j} \Gamma_i \Gamma_j Lk_{ij} + \sum_i \Gamma_i^2 (T_{w,i} + W_{r,i}), \tag{1.1}$$

where Lk_{ij} is the linking number between vortices i and j, W_r is the writhe of the vortex centreline and T_w is the twist of each vortex. Note that both the linking number and writhe can be obtained from a measurement of the vortex tube centrelines alone; however, the twist and global helicity require additional measurements of the flow inside each of the vortex tubes.

Kida & Takaoka (1987, 1988) conducted the first DNS of a trefoil knotted vortex at the vortex Reynolds number Re ($\equiv \Gamma/\nu$, circulation/viscosity) $= 1200$ and observed that H slowly decreases during the whole process. They further found that the decay rate decreases with increasing Re, which seems to suggest that H is conserved at sufficiently high Re. Knotted vortex dynamics did not draw too much attention until the work by Kleckner & Irvine (2013), who experimentally created isolated trefoil knots in water.

https://doi.org/10.1017/jfm.2021.580 Published online by Cambridge University Press

Using high-speed scanning tomography, they measured the topological and geometrical evolution of these knots and observed an initial stretching of the vortex core, as well as the generation of two separate vortex rings after reconnection. Scheeler *et al.* (2014) further observed that the centreline helicity is conserved during the topological change from a single trefoil vortex to two separate vortex rings. In addition, they further simulated the evolution of trefoil knots in a superfluid with the Gross–Pitaevskii equation, where a discrete jump in the centreline helicity across the reconnection is observed. Laing, Ricca & Sumners (2015) analytically demonstrated that total writhe remains conserved under anti-parallel reconnection. Inspired by the studies of Irvine and co-workers, Kerr (2018*c*) numerically studied the evolution of perturbed trefoil knotted vortices and confirmed that the total helicity is conserved before reconnection, followed by a progressive and steady decay after reconnection. Scalo and co-workers (Yu, Chapelier & Scalo 2018; Zhao & Scalo 2019) performed large eddy simulations of the trefoil knotted vortex up to $Re = 20000$ and observed qualitative matches with experiments by Scheeler *et al.* (2014). Recently, Zhao *et al.* (2021) conducted DNS for $Re \leq 6000$ using the adaptive mesh refinement technique and found that H experiences a sudden jump during reconnection at high Re. Xiong & Yang (2019, 2020) developed a method for constructing knotted vortex tubes with finite thickness, arbitrary complexity and tunable twist, and studied the effect of twist on the evolution in resistive magnetohydrodynamic flows. In addition to these experimental and DNS works, there are also some studies on knotted vortex based on the Biot–Savart model, such as Maggioni *et al.* (2010) and Oberti & Ricca (2019).

Although reconnection of knotted vortices has been studied both numerically and experimentally, its underlying mechanism remains rather elusive. For example, it is still unclear how helicity affects the reconnection process, whether helicity remains conserved or not, and what is the conversion mechanism between writhe and twist during helicity evolution. These prompted us to conduct a systematic study of the reconnection of trefoil knotted vortices up to $Re = 12\,000$. The paper is organized as follows. In § 2 we provide details of the initial configuration and numerical set-up. The results for zero initial twist ($T_{w,0} = 0$) cases, including flow visualization, statistics and helicity dynamics, are discussed in §§ 3 and 4. In § 5 the effect of the initial twist on flow evolution is discussed, and, finally, conclusions are drawn in § 6.

2. Initial configuration and numerical set-up

The knotted vortex tube is constructed following Xiong & Yang (2019, 2020). For a given continuous and differentiable closed curve C without vanishing curvature in three-dimensional Euclidean space $\mathbb{R}^3$, its parametric equation is $\boldsymbol{x} = \boldsymbol{c}(s)$, where $\boldsymbol{x} = (x, y, z)$ denotes spatial Cartesian coordinates and $s \in [0, L_C)$ is the arclength parameter with L_C the length of C.

The Frenet–Serret frame on C is

$$\boldsymbol{T}(s) = \partial_s \boldsymbol{c}(s); \quad \partial_s \boldsymbol{N} = \tau \boldsymbol{B} - \kappa \boldsymbol{T}; \quad \kappa \boldsymbol{N} = \partial_s \boldsymbol{T}; \quad \partial_s \boldsymbol{B} = -\tau \boldsymbol{N}, \tag{2.1a–d}$$

where $\boldsymbol{T}$, $\boldsymbol{N}$ and $\boldsymbol{B} \equiv \boldsymbol{T} \times \boldsymbol{N}$ denote the unit tangent, normal and binormal vectors, respectively, and κ is the curvature and τ is the torsion of the curve. The helicity of the knotted vortex tube can be expressed as

$$H = \Gamma^2 \left(W_r + T_w\right), \tag{2.2}$$

where the writhe (figure 1*a*) is

$$W_r = \frac{1}{4\pi} \oint_C \oint_C \frac{[\boldsymbol{N}(s) \times \boldsymbol{N}(s')] \cdot [\boldsymbol{c}(s) - \boldsymbol{c}(s')]}{|\boldsymbol{c}(s) - \boldsymbol{c}(s')|^3} \, \mathrm{d}s \, \mathrm{d}s' \tag{2.3}$$

https://doi.org/10.1017/jfm.2021.580 Published online by Cambridge University Press

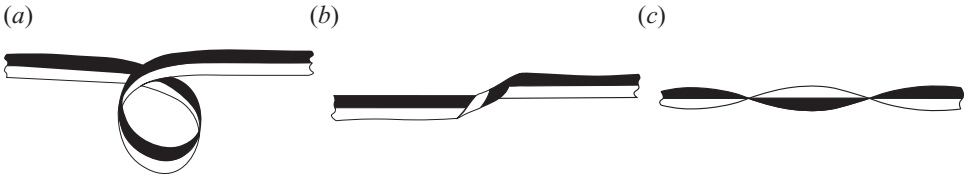


Figure 1. Schematics of (*a*) writhe, (*b*) torsion twist and (*c*) intrinsic twist. Adapted from Moffatt & Ricca (1992) with permission.

and the twist T_w can be further decomposed into (Moffatt & Ricca 1992)

$$T_w = T_t + T_i(L_C), \tag{2.4}$$

with the total torsion (figure 1*b*)

$$T_t = \frac{1}{2\pi}\oint_C \tau \,\mathrm{d}s, \tag{2.5}$$

and the intrinsic twist (figure 1*c*)

$$T_i(s) = \frac{1}{2\pi}\int_0^s \xi(\lambda)\,\mathrm{d}\lambda. \tag{2.6}$$

Here, $\xi(\lambda)$ is the rate of azimuth change along C. Note that W_r and T_t can be uniquely determined once the curve C is defined, and their sum is the self-linking number L_s (Pohl 1968; Moffatt & Ricca 1992). In addition, the twist T_w, as well as the total helicity H, can be tuned by varying the intrinsic twist T_i. For example, by choosing $\xi = -\tau$, one can obtain vortex tubes with zero initial twist $T_{w,0} = 0$.

Note that for a vortex in viscous flows, it is rather difficult or sometimes even impossible to directly measure its twist T_w. In addition, during vortex reconnection, where numerous fine-scale vortex filaments are generated and become tangled with each other, the helicity decomposition based on (2.2) may break down. As an approximation, we define

$$\tilde{T}_w = H/\Gamma^2 - W_r \tag{2.7}$$

as 'generalized twist'.

The parametric equations $\boldsymbol{c}(\zeta) = (c_x(\zeta), c_y(\zeta), c_z(\zeta))$ for the trefoil torus knot (figure 2) are

$$\left.\begin{aligned} c_x(\zeta) &= (R_t + r_t\cos(q\zeta))\cos(p\zeta)), \\ c_y(\zeta) &= (R_t + r_t\cos(q\zeta))\sin(p\zeta)\big), \\ c_z(\zeta) &= -1.5 - r_t\sin(q\zeta), \end{aligned}\right\} \tag{2.8}$$

with $R_t = 1$, $r_t = 0.5$, $p = 2$, $q = 3$ and $\zeta \in [0, 2\pi)$. Note that R_t is also equal to the initial mean radius, defined as $\bar{R} = (1/L_c)\oint_C R(s)\,\mathrm{d}s$. The writhe W_r and the normalized total torsion T_t of the curve, calculated based on (2.3) and (2.5), are 3.52 and 2.48, respectively. Hence, the self-linking number $L_s = W_r + T_t = 6$, which is different from those considered by Scheeler *et al.* (2014), Kerr (2018*c*) and Yu *et al.* (2018) (i.e. $L_s = 3$).

The vorticity field in the curved cylindrical coordinate system is

$$\boldsymbol{\omega} = [\omega_s\boldsymbol{e}_s + \omega_\rho\boldsymbol{e}_\rho + \omega_\theta\boldsymbol{e}_\theta] = \Gamma f(\rho)\left[\boldsymbol{e}_s + \frac{\rho}{1-\kappa\rho\cos\theta}(\xi+\tau)\boldsymbol{e}_\theta\right], \tag{2.9}$$

where ω_s, ω_ρ and ω_θ are the components of $\boldsymbol{\omega}$ in the axial ($\boldsymbol{e}_s$), radial ($\boldsymbol{e}_\rho$) and azimuthal ($\boldsymbol{e}_\theta$) directions, respectively; Γ is the strength of vorticity flux, $f(\rho)$ is vorticity flux

https://doi.org/10.1017/jfm.2021.580 Published online by Cambridge University Press

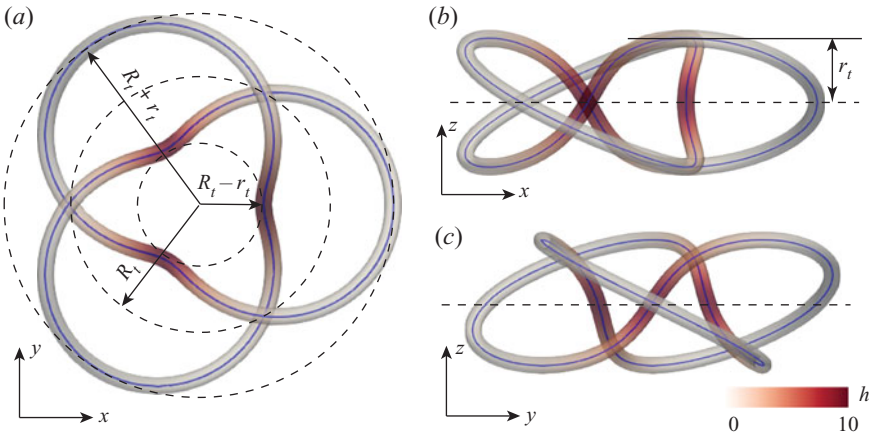


Figure 2. (*a*) Top, (*b*) front and (*c*) side views of the initial configuration of the trefoil knotted vortex (represented by vorticity isosurface at 4 % of maximum initial vorticity colour coded by the helicity density h). Note that $R_t - r_t$ and $R_t + r_t$ are the minimum and maximum knot radii, and the blue lines inside the vortex tube denote the vortex centreline.

distribution with ρ the nearest distance between the centreline and the point where the vorticity is assigned. Note that the axial component $\Gamma f(\rho)\boldsymbol{e}_s$ in (2.9) corresponds to the vector field with a writhe-dependent helicity, and the azimuthal part $\Gamma f\rho(\xi + \tau)\boldsymbol{e}_\theta/(1 - \kappa\rho\cos\theta)$ normal to the central axis represents the twist of vortex lines. The detailed algorithm on how to construct the vorticity field is provided in Xiong & Yang (2019, 2020). In the current study, the strength is set to $\Gamma = 1$, and the vorticity flux distribution f is chosen to be a Gaussian function

$$f(\rho) = \frac{1}{2\pi\sigma^2}\exp\left(-\frac{\rho^2}{2\sigma^2}\right), \tag{2.10}$$

where the standard deviation is set to $\sigma = 1/(16\sqrt{2\pi}) \approx 0.025$. The effective core radius is estimated as $r_e = 2\sigma$, within which the vortex tube contains 95 % of the circulation; hence, the ratio between the mean radius and core size $R_t/r_e = 8\sqrt{2\pi} \approx 20$.

Direct numerical simulation of the incompressible Navier–Stokes equations is carried out in a periodic domain with dimensions $(2\pi)^3$ using a Fourier pseudospectral algorithm in the velocity-vorticity form (Pradeep & Hussain 2004; Yao & Hussain 2020*a*). Time integration is carried out with an explicit third-order Runge–Kutta scheme, while the viscous term is treated exactly with the integrating factor technique (Canuto *et al.* 2012). Time is non-dimensionalized as $t^* = t/(R_t^2/\Gamma)$. In the current study, we first consider the zero initial twist cases ($\xi = -\tau$) at three different vortex Reynolds numbers $Re = 2000$, 6000 and 12 000. In addition, to examine the effect of initial twists, two additional cases with $\xi = 10\pi/L_c$ ($T_w = 7.48$) and $20\pi/L_c$ ($T_w = 22.48$) are considered for $Re = 2000$ and 6000, respectively. Grid points $N^3 = 768^3$, 2048^3 and 4096^3 are employed for $Re = 2000$, 6000 and 12 000, respectively. A grid convergence analysis, reported in Appendix A, clearly demonstrates that the grid resolutions employed here are adequate to capture the flow details. Note that due to limited computational resources, the convergence tests are performed only for $Re = 2000$ and 6000. For $Re = 12\,000$, the adequacy of the numerical resolution is justified by examining the rate of change of the volume-integrated kinetic energy $E = \int_V (\boldsymbol{u}^2/2)\,\mathrm{d}V$ (Archer, Thomas & Coleman 2008; Yao & Hussain 2020*b*), whose balance equation for flow in a triply periodic box is $\mathrm{d}E/\mathrm{d}t = -2\nu\Omega^2$, with $\Omega =$

https://doi.org/10.1017/jfm.2021.580 Published online by Cambridge University Press

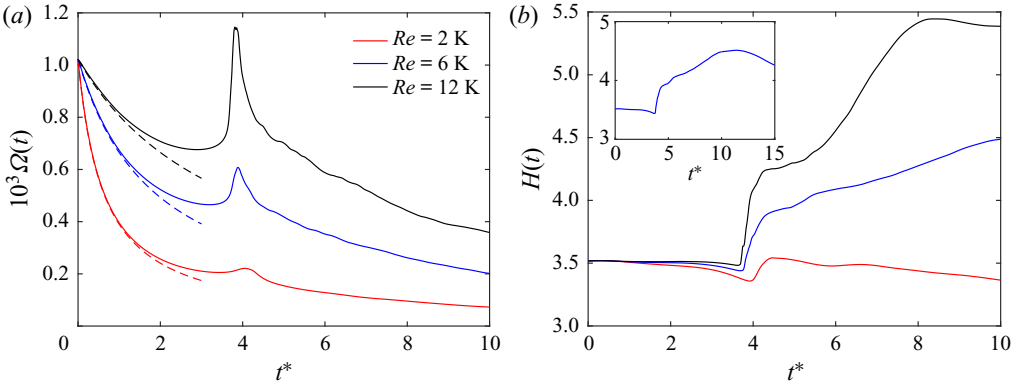


Figure 3. Time evolution of (*a*) enstrophy Ω and (*b*) global helicity H for $Re = 2000$ (red), 6000 (blue) and 12 000 (black). The dashed lines in (*a*) denote $\Omega(t) = \Omega_0 \exp[-\int_0^t (2\nu/\sigma^2)]\,\mathrm{d}t$ with $\sigma = \sqrt{\sigma_0^2 + 2\nu t}$, and the inset in (*b*) shows the long time evolution of $H(t)$ for $Re = 6000$.

$\int_V (\boldsymbol{\omega}^2/2)\,\mathrm{d}V$ being the enstrophy. The maximum relative error between $|\mathrm{d}E/\mathrm{d}t|$ and $2\nu\Omega^2$ is less than 1 % – suggesting the adequacy of the numerical resolution.

3. Flow physics for zero initial twist cases

3.1. *Flow statistics*

Figure 3(*a*) shows the time evolution of enstrophy $\Omega = \int_V (\boldsymbol{\omega}^2/2)\,\mathrm{d}V$ for three different Reynolds numbers. Due to viscous dissipation, the enstrophy initially decays, and the decay rate decreases with increasing Re. For a rectilinear Lamb–Oseen vortex, the rate of enstrophy change is $(1/\Omega)\partial\Omega/\partial t = 2\nu/\sigma^2$ with σ growing as $\sigma(t) = \sqrt{\sigma_0^2 + 2\nu t}$ (Appendix B). Consequently, the enstrophy should follow $\Omega(t) = \Omega_0 \exp[-\int_0^t (2\nu/\sigma^2]\,\mathrm{d}t$. For the trefoil vortex considered here, the initial decrease of Ω also agrees with this prediction, and the agreement deteriorates as Re increases – probably due to enhanced enstrophy production caused by vortex stretching. Note that due to smaller vortex core sizes, the enstrophy decays faster than that observed in Yao & Hussain (2020*b*) for thicker core cases. When reconnection occurs, $\Omega(t)$ experiences rapid growth, which also corresponds to an increase in energy dissipation as $\epsilon = 2\nu\Omega$. The peak of Ω increases with Re, which is due to enhanced vortex stretching and, hence, concomitant higher production. In addition, the time to reach the peak slightly decreases with Re, suggesting that the reconnection happens sooner at higher Re – akin to that observed by Zhao *et al.* (2021). Also, the Ω peak is narrower as the reconnection occurs faster at higher Re. After the peak, the interaction slows down; as a result, the enstrophy experiences a gradual exponential drop – this time the rate increasing with Re, because of more numerous and smaller scales created during reconnection.

The evolution of the global helicity H is shown in figure 3(*b*). Initially, H remains almost constant, and then slightly decreases before reconnection, with the decay rate decreasing with increasing Re due to suppressed viscous dissipation. During and after reconnection, the $H(t)$ behaviour is strongly Re dependent. At $Re = 2000$, H slowly and steadily decays after a slight increase, which is consistent with the observations by Kida & Takaoka (1987) and Kerr (2018*c*). However, at $Re = 6000$, H steadily increases after the jump, which is consistent with the results of Zhao *et al.* (2021). Interestingly, such a helicity jump was

https://doi.org/10.1017/jfm.2021.580 Published online by Cambridge University Press

not clearly observed by Scheeler *et al.* (2014) and Kerr (2018*c*), which might be due to different initial conditions employed in their studies. At $Re = 12\,000$, H rapidly increases and then finally becomes saturated. Compared with its initial value, the peak of H for the $Re = 12\,000$ case increases by approximately 50 %. Note that despite the fact that H increases for the two higher Re cases after reconnection, it eventually decays. The inset in figure 3(*b*) provides a longer time evolution of H for $Re = 6000$, showing that H starts to decrease at $t^* \approx 11.45$. Nevertheless, the transient growth of $H(t)$, which is expected to further increase at higher Re, is quite surprising and will be discussed in detail later.

3.2. *Flow structures*

Figure 4 shows the time progression of flow structures visualized based on vorticity magnitude isosurface $|\boldsymbol{\omega}|$ for different Re cases. Note that to capture the evolution details, a relatively low threshold $|\boldsymbol{\omega}| = 0.04\omega_0$ is chosen, with ω_0 being the maximum vorticity magnitude at $t^* = 0$. The knotted vortex rotates counterclockwise as it moves along the z-direction. During this process, the vortex is deformed so that the neighbouring parts of the tube become anti-parallel and collide with each other due to self-induction; and then reconnect in a manner similar to previous studies, e.g. Melander & Hussain (1988) and Boratav *et al.* (1992). Due to symmetry, three reconnections occur simultaneously. Note that it is different from those reported by Kleckner & Irvine (2013) and Kerr (2018*c*), where the trefoil knotted vortex is perturbed and only one reconnection occurs at a time. The reconnected parts (called bridges) combine with other parts – forming two separated vortex rings, i.e. a small leading ring and a large trailing ring (hereinafter, referred to as SLR and LTR, respectively). Both SLR and LTR continuously rotate as they propagate upward. Different from quantum reconnection, the viscous reconnection is not complete, and parts of the initial vortex tube are left over as threads. As the two rings propagate and rotate at different speeds, the threads undergo continuous stretching and finally dissipate due to viscous effects. In addition, although the core sizes are very small, the SLR and LTR experience strong core dynamics (Melander & Hussain 1994). For example, the coiling of vortex lines induce axial flows in the core, and their interactions lead to the generation of a low vorticity bubble along the vortex tubes (see the gaps of vorticity magnitude isosurface in LTR at $t^* = 9.36$ for $Re = 2000$).

The dynamics at high Re are quite similar to that at low Re, and the main apparent difference is the generation of more small scales due to intense vortex stretching and weak viscous dissipation. Some of these small scales wrap around the newly formed vortex rings, akin to that observed by Yao & Hussain (2020*b*) for high Re anti-parallel vortex reconnection and by Pradeep & Hussain (2010) for vortex–turbulence interaction. Another interesting feature is that although the knotted vortex initially has predominately positive helicity density, some segments acquire negative helical density during reconnection and these negative structures become more prominent and persist longer at high Re. In addition, the positive and negative helical structures appear alternatively at late time, which implies the presence of strong twist oscillations along the vortex tubes. In § 4 we will show that these newly generated helical structures are the main cause for the post-reconnection helicity growth at higher Re (figure 3).

3.3. *Properties of vortex centrelines*

Before going into the details of vortical structures, we first examine the evolution of the vortex core centreline (axis). Note that as vortex lines typically do not align along the vortex core (Schoppa & Hussain 2002; Yao & Hussain 2018), they cannot be employed

https://doi.org/10.1017/jfm.2021.580 Published online by Cambridge University Press

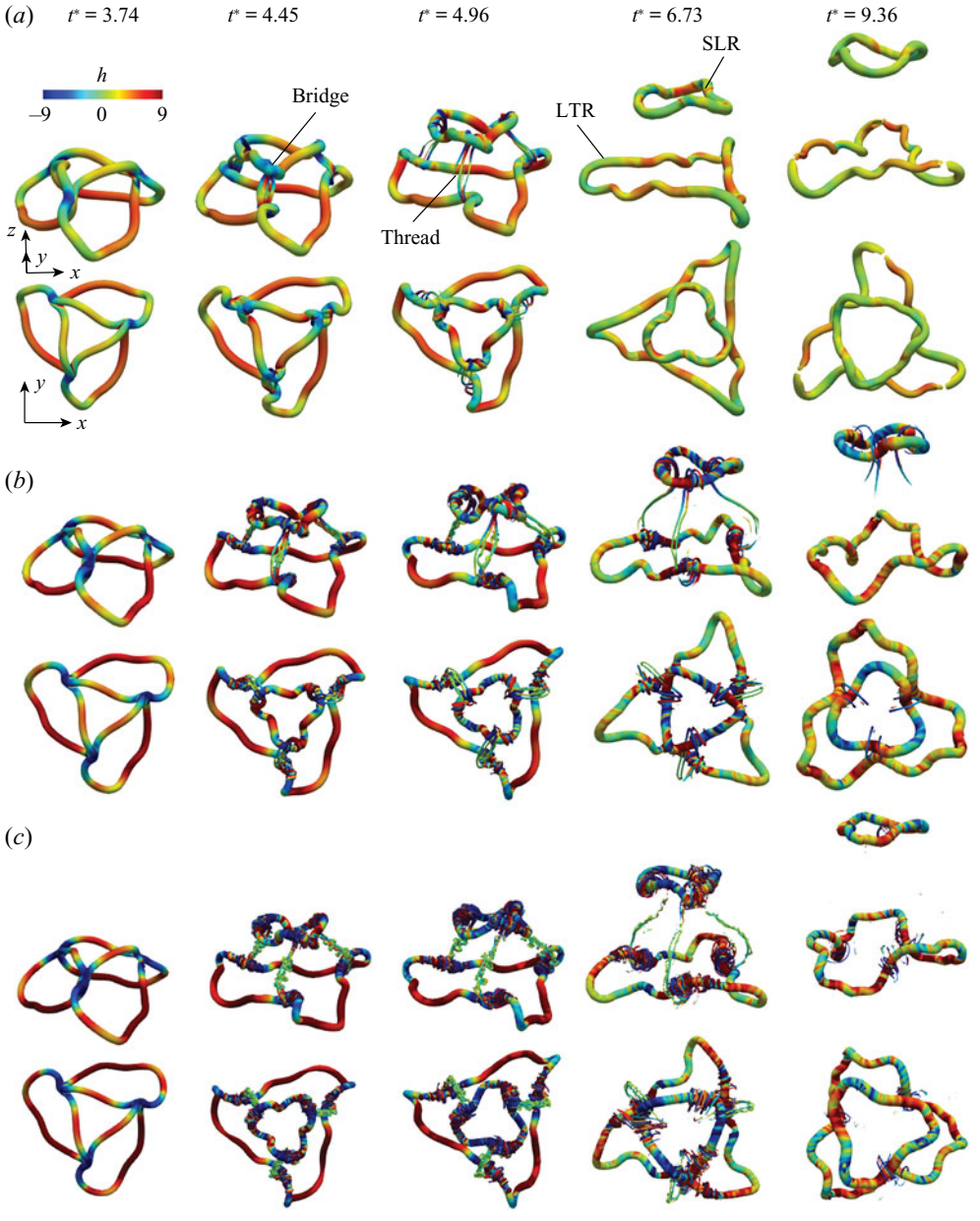


Figure 4. Evolution of flow structures represented by vorticity isosurface at 4 % of maximum initial vorticity ($|\boldsymbol{\omega}| = 0.04\omega_0$) shaded with helicity density $h = \boldsymbol{u} \cdot \boldsymbol{\omega}$ for (*a*) $Re = 2000$, (*b*) 6000 and (*c*) 12 000.

to represent the vortex core centreline. How to identify the vortex core axis is still an open question, and numerous approaches have been proposed (Sujudi & Haimes 1995; Tian *et al.* 2018). Here, we use the method developed by Levy, Degani & Seginer (1990) based on the normalized helicity density $\boldsymbol{u} \cdot \boldsymbol{\omega}/(|\boldsymbol{u}|\,|\boldsymbol{\omega}|)$ and implemented in Paraview by Sadlo *et al.* (2019). The use of normalized helicity density is based on the argument that the angle between the velocity and vorticity vectors is typically minimal near the vortex core axis. It can filter out the regions of low vorticity, as well as regions of high vorticity

https://doi.org/10.1017/jfm.2021.580 Published online by Cambridge University Press

but low velocity, particularly where the angle between the velocity and vorticity vectors is large. This method works very well in extracting the vortex centrelines, except for the short period when reconnection occurs and the vortex core is non-unique. Figure 5 shows the corresponding centrelines of the structures shown in figure 4, which represent well the vortex knot before reconnection, and SLR and LTR after reconnection. Furthermore, Kelvin waves are observed after reconnection, and the nonlinear interaction among them creates waves of shorter and shorter wavelengths – one of the main mechanisms for energy cascade in quantum reconnection (Baggaley & Barenghi 2011; Fonda *et al.* 2014).

Based on the tracked vortex centrelines, several interesting quantities can be measured. The first one is the length of the vortex centreline l_c. From the local induction approximation of the Biot–Savart model, the total length l_c of the vortex is proportional to the kinetic energy $E(t)$ (Alamri, Youd & Barenghi 2008). As energy is 'dissipated' as sound radiation during reconnection, a decrease in the total length has been observed from quantum reconnection (Proment & Krstulovic 2020). Figure 6 shows the evolution of lengths for the vortex knot before reconnection and SLR and LTR and their sum after reconnection. Consistent with that observed in Scheeler *et al.* (2014) for a quantum trefoil knot, the total length $l_c(t)$ continuously increases before reconnection, suddenly drops during reconnection, and remains almost constant after reconnection. In addition, before reconnection $l_c(t)$ is almost identical for different Re, but after reconnection it slightly decreases as Re increases. Namely, it is approximately 25 %, 18 % and 15 % longer than its initial length L_c for $Re = 2000$, 6000 and 12 000, respectively. Both the lengths of the large (l_c^l) and small (l_c^s) rings decrease as Re increases, and their ratio (l_c^l/l_c^s) slightly increases with Re, which corresponds to approximately 2.0, 2.21 and 2.29 for $Re = 2000$, 6000 and 12 000, respectively. The shorter in total length l_c after reconnection at high Re is associated with an earlier reconnection. Besides, it seems that the change in l_c during reconnection is qualitatively linked to the total energy loss during reconnection: as the energy dissipation is reduced at high Re, the drop in total length Δl is also smaller – akin to that found by Proment & Krstulovic (2020).

The moment of vorticity for a vortex knot in a fluid at rest at infinity is related to the impulse (Batchelor 2000)

$$\boldsymbol{I} \equiv \frac{1}{2}\iiint_{\mathbb{R}^3} \boldsymbol{x}\times\boldsymbol{\omega}(\boldsymbol{x})\,\mathrm{d}V \approx \frac{1}{2}\iiint_{\Omega} \boldsymbol{x}\times\boldsymbol{\omega}(\boldsymbol{x})\,\mathrm{d}V, \tag{3.1}$$

which can be approximated by the integral over the periodic domain for the very thin vortex tubes. As a theoretical estimation for the thin vortex filament, substituting $\boldsymbol{\omega}\,\mathrm{d}V = \Gamma\,\mathrm{d}\boldsymbol{c}$ to (3.1) yields

$$\boldsymbol{I} = \Gamma\boldsymbol{S}, \tag{3.2}$$

where $\boldsymbol{S} = \oint_c \boldsymbol{c}\times\mathrm{d}\boldsymbol{c}/2$ is the directed area enclosed by the curve (Wu, Ma & Zhou 2007). Following (3.2), the trefoil knotted vortex specified based on (2.8) has an initial impulse $\boldsymbol{I} = (0, 0, 4.5\pi)$, which is very close to the value of $(0, 0, 14.16)$ numerically calculated over the periodic domain V ((3.1)) for the finite thickness case. Since the impulse is a motion invariant, it can be employed to characterize the evolutionary geometry of vortex knots (Xiong & Yang 2019).

Figure 7 shows the evolution of the third component (S_3) of the directed area enclosed by the vortex centrelines for the vortex knot before reconnection, and for SLR and LTR and their sum after reconnection. Note that the other two components are negligible and, hence, are not shown. For $Re = 2000$, S_3 continuously increases with time. As $\boldsymbol{I}$ is invariant, the increase of S_3 is mainly due to the decrease in circulation Γ through viscous

https://doi.org/10.1017/jfm.2021.580 Published online by Cambridge University Press

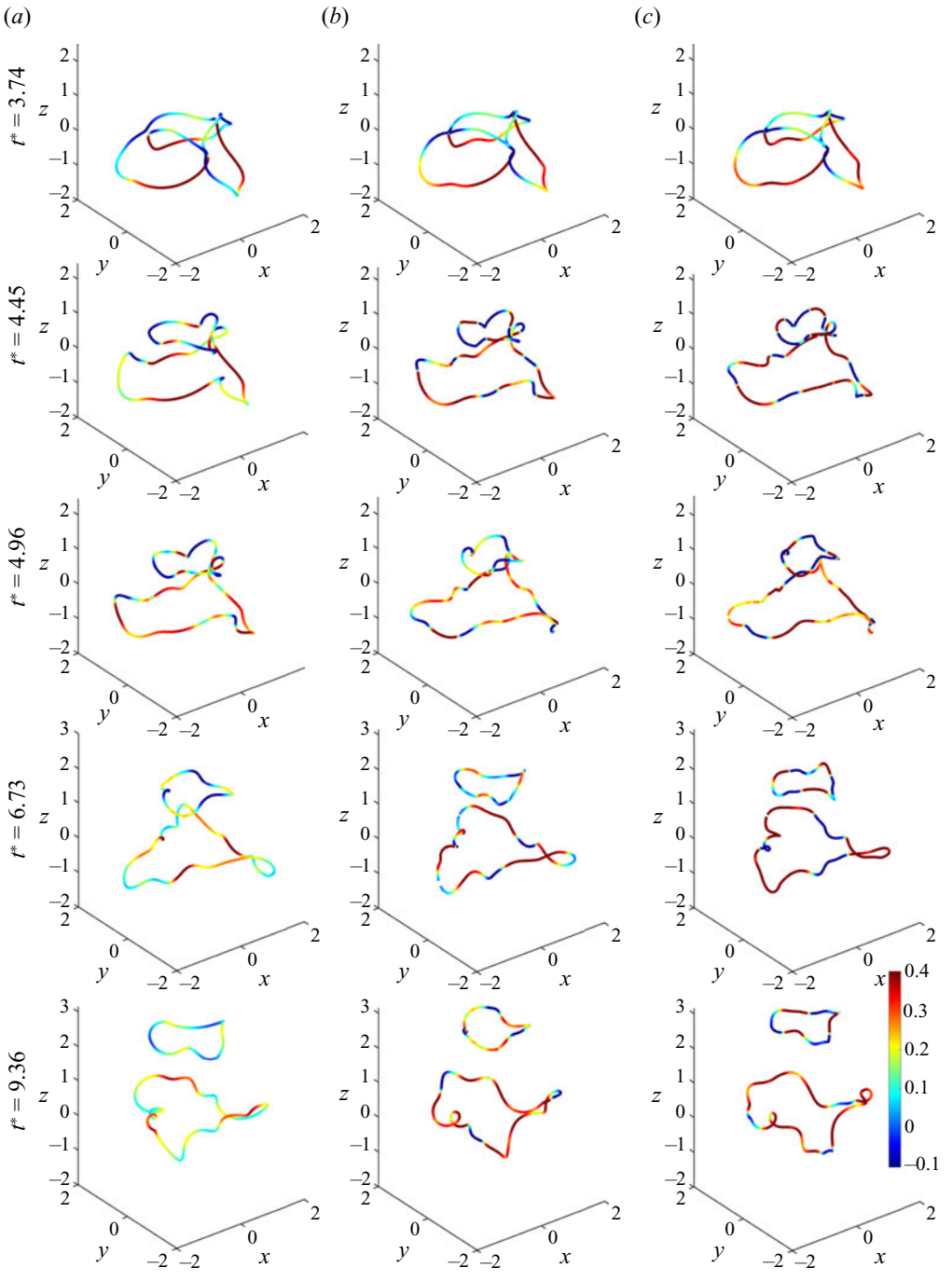


Figure 5. Evolution of extracted vortex centreline (shaded with centreline helicity density $h_c = \boldsymbol{u} \cdot \boldsymbol{T}$) for structures shown in figure 4: (*a*) $Re = 2000$, (*b*) 6000 and (*c*) 12 000.

https://doi.org/10.1017/jfm.2021.580 Published online by Cambridge University Press

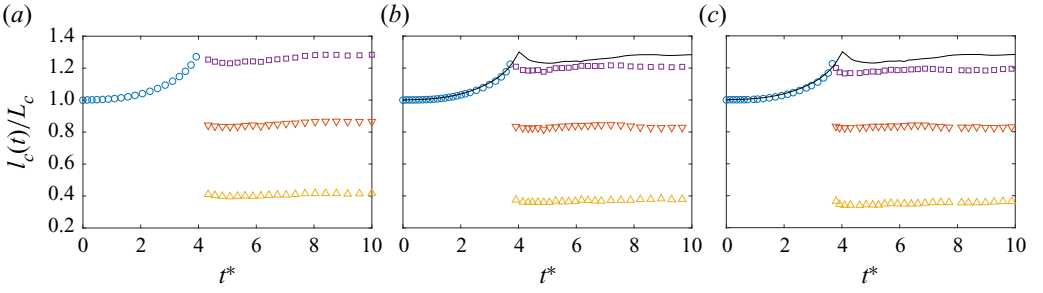


Figure 6. Time evolution of the normalized total length l_c/L_c for the vortex knot before reconnection (circle), and for SLR (△), LTR (▽) and their sum (□): (*a*) $Re = 2000$, (*b*) 6000 and (*c*) 12 000. Note that the total length for the $Re = 2000$ case (solid lines) is shown in (*b*,*c*) as a reference.

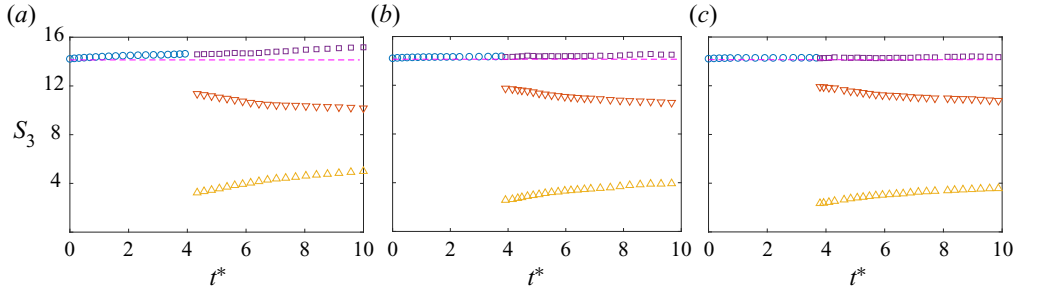


Figure 7. Time evolution of the third components of the directed area enclosed by the vortex centrelines S_3 for the vortex knot before reconnection (circle), and for SLR (△), LTR (▽) and their sum (□): (*a*) $Re = 2000$, (*b*) 6000 and (*c*) 12 000. Note that the dashed lines represent the theoretical value 4.5π.

cross-diffusion, which decreases with increasing *Re*. Therefore, S_3 is better conserved at high *Re*; and the difference between the calculated value and the theoretical prediction is within 1 % for $Re = 12\,000$. In addition, due to the mutual induction between SLR and LTR, S_3 continuously increases and decreases for SLR and LTR, respectively – similar to those observed for the leap-frogging of two co-axial vortex rings (Mariani & Kontis 2010; Scheeler *et al.* 2017). The rate of change of S_3 decreases as the two rings separate.

Figure 8 shows the mean radius $\bar{R}$ and z-location $\bar{z}$ for the vortex knot before reconnection, and for SLR and LTR after reconnection, defined as

$$\bar{R}(t) = \frac{1}{L_c}\oint_C R(s)\,\mathrm{d}s, \tag{3.3}$$

$$\bar{z}(t) = \frac{1}{L_c}\oint_C z(s)\,\mathrm{d}s. \tag{3.4}$$

Similar to the total length l_c, the mean radius of the vortex knot $\bar{R}$ continuously increases before reconnection and is almost identical among different *Re* cases. The mean radius for the small ring after reconnection $\overline{R}^s$ slightly increases with time, which is consistent with the increases of S_3 (figure 7). In addition, similar to the total length l_c^s shown in figure 6, $\overline{R}^s$ decreases with increasing *Re*. The mean radius of the large ring $\overline{R}^l$ slightly increases before it decreases, with the peak occurring earlier as *Re* increases. The difference in the mean radius for the large ring $\overline{R}^l$ decreases as *Re* increases and becomes indistinguishable between $Re = 6000$ and 12 000 cases.

https://doi.org/10.1017/jfm.2021.580 Published online by Cambridge University Press

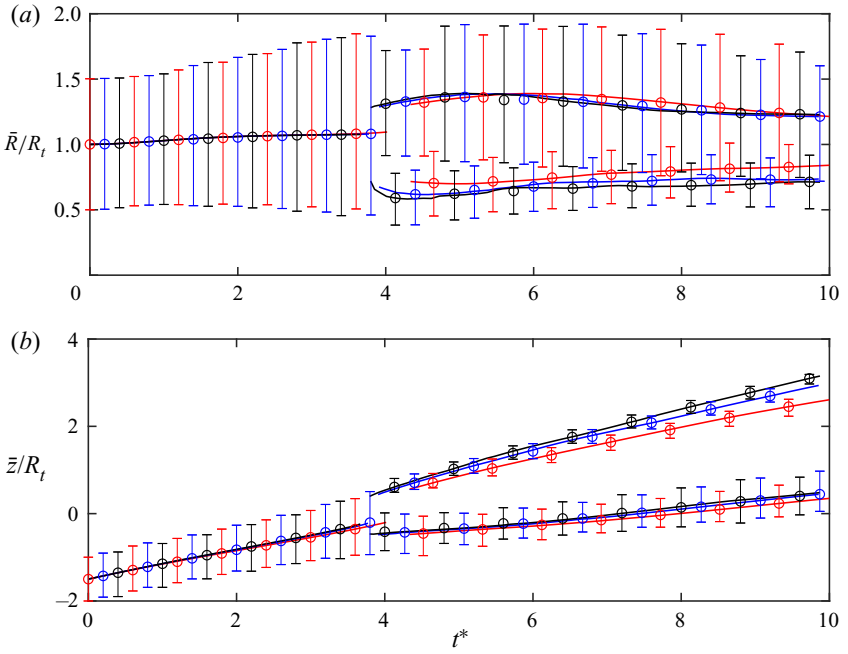


Figure 8. (*a*) Mean radius $\bar{R}$ and (*b*) mean z-location $\bar{z}$ for the vortex knot before reconnection, and for SLR and LTR for $Re = 2000$ (red), $Re = 6000$ (blue) and $Re = 12\,000$ K (black). The bars denote the range between minima and maxima.

Re	v_t	v_s	v_b
2000	0.314	0.362	0.145
6000	0.329	0.414	0.156
12 000	0.334	0.444	0.162

Table 1. Fitted values of the propagation velocity for the vortex knot before reconnection (v_t) and SLR (v_s) and LTR (v_b) after reconnection.

As discussed above, the vortex knot continuously propagates upward during the interaction. Similar to the mean radius, the mean z-location mainly differs for the small ring after reconnection. The propagation velocities for the vortex knot before reconnection, and for SLR and LTR, obtained from linear fitting, are shown in table 1. In general, as Re increases, the vortex core size is smaller due to reduced diffusion; hence, the propagation velocities also increase (Dyson 1893). The propagation velocity for the small ring increases significantly, which is partially due to a reduced mean radius as shown in figure 8(*a*).

Another interesting question is the separation distances $\delta(t)$ before and after reconnection (Zuccher *et al.* 2012). Based on the assumption that reconnection is a localized event and the circulation Γ is the only relevant dimensional quantity involved, we have

$$\delta(t) = A^{\pm}(\Gamma|t - t_0|)^{1/2}, \tag{3.5}$$

where t_0 is the reconnection time, and A^- and A^+ are dimensionless factors for pre- and post-reconnection, respectively. This scaling follows dimensional analysis and has been observed for reconnection of line vortices (Kimura & Moffatt 2017) and also for

https://doi.org/10.1017/jfm.2021.580 Published online by Cambridge University Press

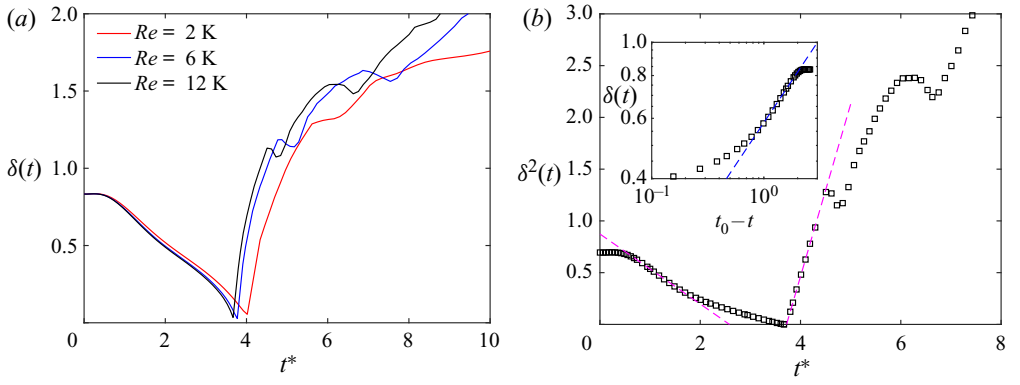


Figure 9. Time evolutions of (*a*) separation distance $\delta(t)$ and (*b*) $\delta^2(t)$ for 12 000. In panel (*b*) the dashed lines indicate linear scaling for pre- and post-reconnection, and the inset is δ as a function of $|t - t_0|$ for pre-reconnection.

Re	a^-	t_0^-	a^+	t_0^+
2000	0.56	2.77	1.05	4.09
6000	0.58	2.62	1.20	3.80
12 000	0.58	2.58	1.29	3.72

Table 2. Fitted values of the prefactors $a^\pm$ and $t_0^\pm$ for the minimum distance scaling $\delta(t) \sim a^\pm |t - t_0^\pm|^{1/2}$. The superscript $\pm$ stands for before ($-$) and after ($+$) the reconnection, respectively.

reconnection of quantized vortices (Fonda *et al.* 2014; Villois, Proment & Krstulovic 2017). Our recent results on thin core vortices show that such 1/2-power scaling is also valid for classical viscous reconnection (Yao & Hussain 2020*a*,*c*).

Figure 9(*a*) displays the evolution of $\delta(t)$ for vortex knot before reconnection and between SLR and LTR after reconnection, with (*b–d*) showing the corresponding $\delta^2(t)$. During the initial phase of forming anti-parallel configuration, $\delta(t)$ slowly varies. Then, it rapidly decreases as the perturbed vortex tubes approach each other due to self-induction. A slight difference in the evolution of $\delta(t)$ can be observed among different Re cases, indicating a weak Re effect on the pre-reconnection evolution. In general, $\delta(t)$ decreases more rapidly as Re increases, which is mainly due to a high self-induced velocity associated with a smaller vortex core size and radius of curvature (Yao & Hussain 2020*a*). The distinct agreement with linear scaling for $\delta^2(t)$ at the early time suggests that $\delta(t) \sim a^-(t_0^- - t)^{1/2}$, with a^- the constant prefactors for pre-reconnection corresponding to $A^-\Gamma^{1/2}$ in (3.5), and t_0^- the critical time when $\delta \to 0$. The values of a^- and t_0^- for different Re obtained from linear fitting on $\delta^2(t)$ during $0.5 < t < 2$ are listed in table 2. As the circulation remains almost constant at $\Gamma = 1$ during this phase, the dimensionless prefactor $A^- \approx a^-$ and is quite close to that reported in Villois *et al.* (2017) for a quantized trefoil vortex knot. Note that $\delta^2(t)$ slowly deviates from linear scaling when $\delta \sim O(\sigma)$. The deviation happens earlier at small Re – due to the more rapid increase of the core size caused by higher viscous diffusion.

After reconnection, a clear linear scaling for $\delta^2(t)$ can be observed (figure 9*b–d*). Hence, $\delta \sim a^+(t - t_0^+)^{1/2}$ scaling also holds in the post-reconnection phase. A fit in the linear region gives $t_0^+ \approx 4.09$, 3.80 and 3.72, and $a^+ = 1.05$, 1.20 and 1.29 for $Re = 2000$,

https://doi.org/10.1017/jfm.2021.580 Published online by Cambridge University Press

6000 and 12 000, respectively. Consistent with previous studies (Villois *et al.* 2017), a^+ is always larger than a^-, indicating that the vortices separate much faster than when they approach each other. Compared with the pre-reconnection phase, the *Re* effect on $\delta(t)$ is more apparent during the post-reconnection. It is because, in classical fluids, the dynamics of reconnection, such as the reconnection time and the circulation transfer rate, strongly depends on viscosity ν. Reconnection is typically faster and more complete at higher *Re* (Hussain & Duraisamy 2011; Yao & Hussain 2020*a*). When the two vortex rings move sufficiently far apart, the $1/2$ scaling breaks down, and the deviation from $1/2$ occurs earlier for higher *Re* – due to stronger Kelvin waves. Note that although, on average, the two vortex rings travel almost at a constant speed, the crossover between the $t^{1/2}$ to t^1 scalings for $\delta(t)$ suggested by Galantucci *et al.* (2019) is not observed here. It is mainly because, due to the strong variation of local curvature, each segment of the vortex ring travels at a different speed – evident from the large variation in the z-location, particularly for LTR (figure 8*b*).

4. Helicity dynamics

4.1. *Centreline helicity, Writhe, torsion and self-link number*

For sufficiently thin vortex tubes with minimal vorticity variation across the cross-section, the total helicity is encoded completely in the flow along the centreline of the vortex tube (Bretherton 1970; Scheeler *et al.* 2017); hence,

$$H_c = \sum_i \Gamma_i \oint_{C_i} \boldsymbol{u}(s) \cdot \boldsymbol{T}(s)\, \mathrm{d}s, \tag{4.1}$$

where $h_c = \boldsymbol{u} \cdot \boldsymbol{T}$ is the centreline helicity density and $\boldsymbol{T}$ again denotes the unit tangential vector along the vortex centreline C. The centreline helicity H_c is sometimes used to represent the writhe helicity, which is based on the assumption that the twist helicity is dissipated rather rapidly, particularly for a very thin vortex (Scheeler *et al.* 2014).

Figure 10(*a*,*c*,*e*) show centreline helicity H_c for the vortex knot before reconnection and for SLR and LTR and their sum after reconnection. In addition, the global helicity H and the helicity for SLR and LTR ($H^s = \int_{V^s} h\, \mathrm{d}V^s$ and $H^l = \int_{V^l} h\, \mathrm{d}V^l$ with V^s and V^l denoting the volume occupied by SLR and LTR) are also included for comparison. Note that when calculating H_c, we assume the circulation remains the same as the initial value Γ. Due to limited viscous cross-diffusion, particularly at high *Re*, this assumption should be valid before reconnection. As reconnection in viscous flows is not complete, the circulations of the bridges in the SLR and LTR are smaller than Γ after reconnection – due to the presence of the remnant threads. However, compared with other unreconnected parts in SLR and LTR, where the circulation remains unchanged as Γ, the bridge is rather short. Hence, on the average, it should still be acceptable to assume that the SLR and LTR have constant circulation Γ after reconnection. The constant circulation assumption is also employed for calculating writhe helicity $\Gamma^2 W_r$. It can be seen that H_c is almost identical to H for the vortex knot before reconnection – confirming that H_c is a reasonably good approximation for H.

After reconnection, H_c experiences oscillations, which indicates that the axial flows along the vortex rings grow and annihilate. In addition, H_c deviates from H, presumably for two main reasons. First, reconnection causes strong core deformation near the interaction region, such as forming vortex sheets; as a result, the vortex core becomes irregular with a strong vorticity variation. Second, as shown in figure 4, the threads, which are polarized,

https://doi.org/10.1017/jfm.2021.580 Published online by Cambridge University Press

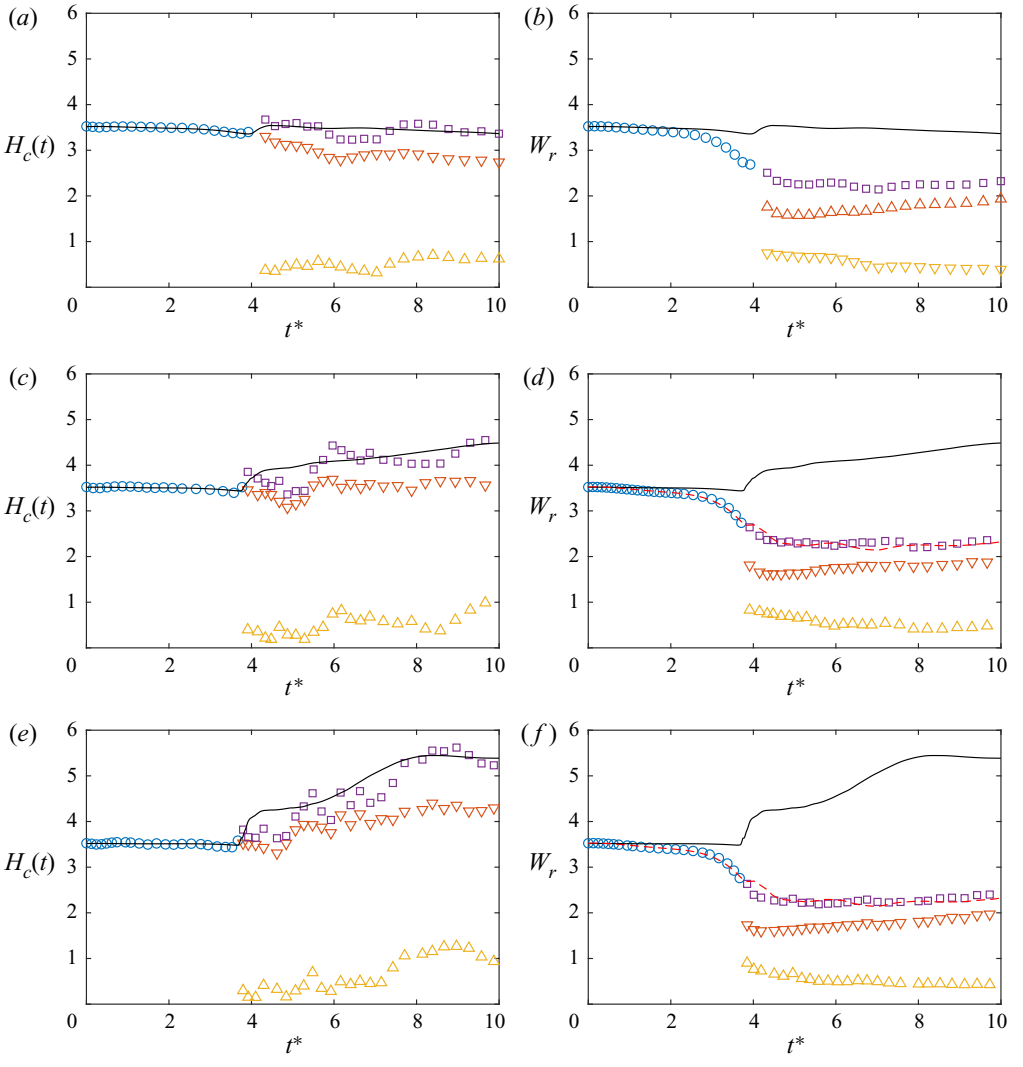


Figure 10. Time evolutions of (*a*,*c*,*e*) the centreline helicity H_c and (*b*,*d*,*f*) the writhe W_r for the vortex knot before reconnection (circle), and for SLR (△), LTR (▽) and their sum (□): (*a*,*b*) $Re = 2000$, (*c*,*d*) 6000 and (*e*,*f*) 12 000. Note that the black solid lines represent the global helicity H, and the black dashed and dash–dotted lines in (*a*,*c*,*e*) represent the total helicity for LTR and SLR, respectively, and the red dashed lines in (*d*,*f*) denote W_r for $Re = 2000$.

also contain a significant amount of helicity density which is excluded by H_c. As expected, the deviation between H_c and H becomes severe as Re increases. Nevertheless, H_c can successfully capture the trend of H for both rings. For SLR, H_c (and also H^s) always grows with time, and the rate of growth increases with Re. For $Re = 2000$, H_c (and H^l) for LTR is found to decrease with time; however, at $Re = 12\,000$, it reverses and slightly increases at late time. Due to viscous damping, H_c becomes less oscillated at late time. Besides, as the vortex core of the two rings becomes regular (i.e. circular) and threads become weaker due to viscous diffusion, H_c eventually agrees with H again. Note that the increase in H_c after reconnection is different from the constant H_c observed in the experiment by Scheeler *et al.* (2014), presumably for two main reasons. First, as shown

https://doi.org/10.1017/jfm.2021.580 Published online by Cambridge University Press

in figure 5, strong oscillations appear in axial velocity along the vortex tubes. There might be some inaccuracy for measuring the centreline helicity density h_c in the experiment. Second, different from three simultaneously reconnections for the ideal trefoil vortex knot considered here, there is only one reconnection at a time in the experiment, as the vortex knot is perturbed. Hence, the increase of H_c in the experiment may not be so distinct and sharp.

Figure 10(b,d,f) show the writhe W_r calculated using (2.3) for the vortex knot before reconnection, as well as for SLR, LTR and their sum after reconnection. As the numerical computation of writhe is very sensitive to small-scale noise in the extracted centreline, a local smoothing filter similar to that used in Scheeler *et al.* (2014) is applied to the raw data (only for the small and large rings after reconnection). Before reconnection, W_r continues to decrease, and after reconnection it has a big drop (but still remains continuous) during the reconnection. Note that the behaviour of W_r here is similar to that observed for reconnections in superfluids (Scheeler *et al.* 2014; Proment & Krstulovic 2020). We note with interest that Laing *et al.* (2015) proved that W_r should be conserved during reconnection of two ideal anti-parallel vortex segments. After reconnection, SLR and LTR are being stretched and compressed, respectively. As a consequence, W_r continuously increases/decreases for the SLR/LTR, but their sum remains roughly constant. It is interesting to observe that W_r seems to be Re independent, and the total drop of W_r is $\Delta W_r \sim 1\Gamma^2$. Scheeler *et al.* (2014) found that ΔW_r strongly depends on the geometry of the trefoil knot, such as the radius to core size ratio R_t/r_e. Note that from figure 10, it is also clear that H_c can not be employed to approximate the writhe helicity $\Gamma^2 W_r$, because the assumption that the twist helicity is dissipated rather rapidly in a thin vortex is no longer valid during viscous reconnection – to be discussed in detail later.

Dramatic helicity change is typically associated with topological changes, but we observe a gradual change in both global and writhe helicities (even when reconnections are not taking place). Because the centreline topology is not altered before reconnection, the major writhe-helicity changes should be attributed to geometric deformations of the vortex – coiling or uncoiling. As suggested by Scheeler *et al.* (2017), during vortex evolution, helicity can transfer between writhe and twist; for example, writhe is increased through coiling or decreased through straightening. This helicity conversion mechanism can explain the writhe evolution observed here. Before reconnection W_r decays faster than the global helicity. This is because, as initially the vortex knot undergoes stretching, part of the writhe helicity is converted to twist helicity. After reconnection, when the two vortex rings form, SLR is stretched by the LTR, hence, its writhe helicity is continuously transferred into twist helicity. On the other hand, as LTR is under compression, its W_R slightly increases. In addition, this conversion mechanism is inviscid, which explains why the evolution of writhe is almost Re independent.

Figure 11 further shows the torsion T_t (2.5) and self-linking number $L_s \equiv W_r + T_s$ for the vortex knot before reconnection, and also for SLR and LTR at $Re = 12\,000$. (Note that the results for $Re = 2000$ and 6000 are quite similar and, hence, are not shown for brevity.) Before reconnection T_t continues to increase and L_s remains constant. A similar conservation of L_s has also been reported by Kerr (2018*b*) for the evolution of coiled vortex rings. To avoid confusion, note that T_t is equivalent to 'T_w' defined in Kerr (2018*b*, *c*). During reconnection, when the vortex knot undergoes dramatic changes in topology, T_t and L_s also change abruptly, which is different from the torsion conservation for the ideal anti-parallel reconnecting segments in Laing *et al.* (2015). Note that the integer L_s jumps discontinuously through ± 1 as a curve passes through a configuration containing a point of inflexion (Moffatt & Ricca 1992). Due to the presence of three additional inflexion points, the initial L_s for our configuration is 6, which is larger than those employed by Scheeler

https://doi.org/10.1017/jfm.2021.580 Published online by Cambridge University Press

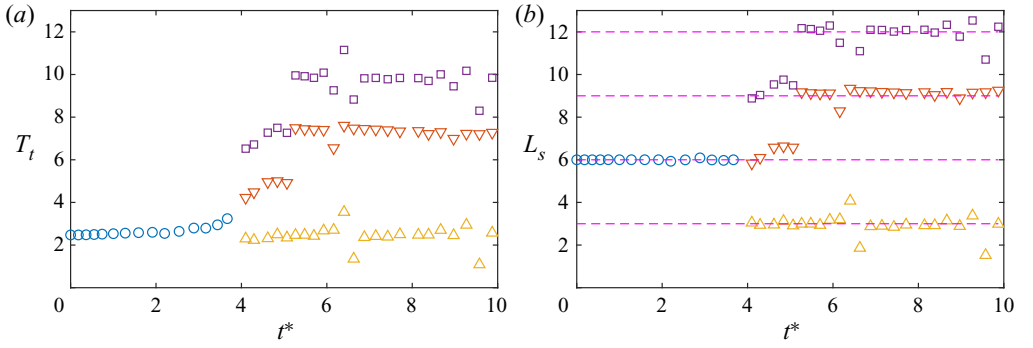


Figure 11. Time evolution of (*a*) the torsion T_t and (*b*) the self-link number L_s for the vortex knot before reconnection (circle), and for SLR (△), LTR (▽) and their sum (□) at $Re = 12\,000$.

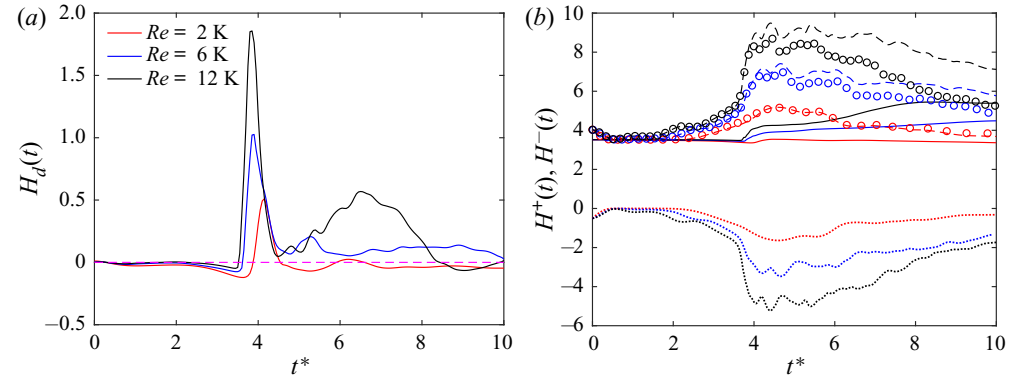


Figure 12. Time evolution of (*a*) helicity dissipation H_d and (*b*) $H^{\pm}$ for $Re = 2000$ (red), 6000 (blue) and 12 000 (black). Note that the circles in (*b*) denote $-H^-(t) + H(0)$, with $H(0) = 3.52$ the initial global helicity.

et al. (2014) and Yu *et al.* (2018) (i.e. $L_s = 3$). Owing to the tri-symmetry of the trefoil knot, the curve deformation during the reconnection involves passage through three inflexional configurations, and self-linking numbers for the two unlinked rings become $L_s = 6 \pm 3$. After reconnection, T_t for the small/large rings slightly increases/decreases with time, and L_s for the small and large rings remains almost constant at 3 and 9, respectively. Moreover, the numerical calculation of T_t is very sensitive at the inflexional configuration for which T_t is discontinuous by ± 1; so T_t and L_k have some notable oscillations in figure 11.

4.2. *Transient helicity growth*

An important question is why global helicity H increases after reconnection for high Re cases. The governing equation for the helicity density h is

$$\frac{\mathrm{D}h}{\mathrm{D}t} = \underbrace{-\boldsymbol{\omega}\cdot\boldsymbol{\nabla}(p/\rho - \boldsymbol{u}^2/2)}_{production} + \underbrace{\nu\nabla^2 h}_{diffusion} - \underbrace{2\nu\boldsymbol{\omega}\cdot(\boldsymbol{\nabla}\times\boldsymbol{\omega})}_{dissipation}, \tag{4.2}$$

where the terms on the right-hand side are the helicity production, diffusion and dissipation, respectively (Kerr 2018*a*); $\boldsymbol{\omega}\cdot(\boldsymbol{\nabla}\times\boldsymbol{\omega})$ is the so-called 'superhelicity' (Brissaud *et al.* 1973; Hide 1989; Scheeler *et al.* 2014). Note that both helicity production and diffusion terms vanish when integrated over the periodic computational domain.

https://doi.org/10.1017/jfm.2021.580 Published online by Cambridge University Press

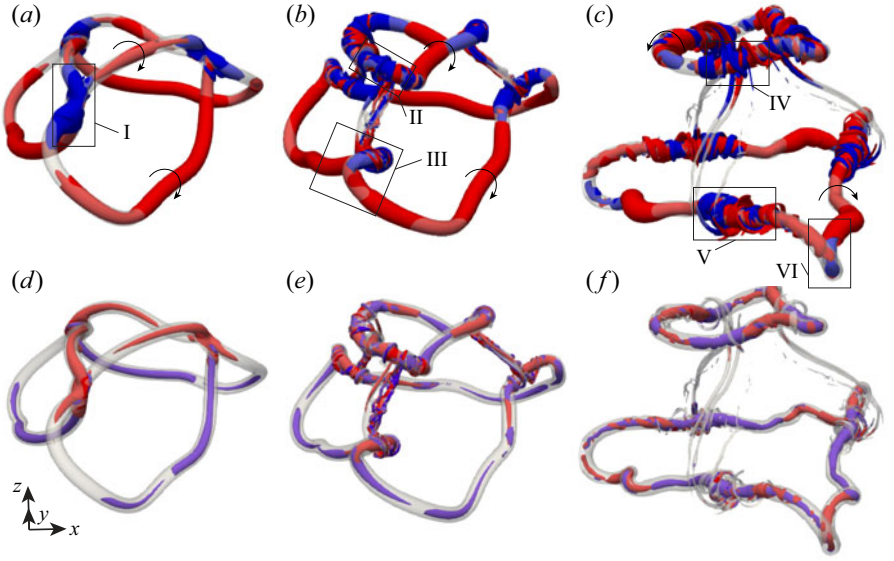


Figure 13. Isosurface of (*a–c*) helicity density $h = \boldsymbol{u} \cdot \boldsymbol{\omega}$ and (*d–f*) helicity dissipation $h_d = -2\nu\boldsymbol{\omega} \cdot (\nabla \times \boldsymbol{\omega})$ for $Re = 6000$ at: (*a*,*d*) $t^* = 3.74$, (*b*,*e*) $t^* = 4.29$ and (*c*,*f*) $t^* = 6.01$. Note that the red and blue colours denote positive and negative of 5 % of the maximum value, and the transparent (grey) isosurface represents $|\boldsymbol{\omega}| = 0.04\omega_0$. The black arrows indicate the direction of vortex rotation.

Therefore, the variation of H is purely due to viscous dissipation $H_d = -2\nu \int_V \boldsymbol{\omega} \cdot (\nabla \times \boldsymbol{\omega})\,\mathrm{d}V$. As H is not positive-sign definite, H_d – different from energy or enstrophy dissipation – can be either positive or negative. However, as shown later in figure 13(*d–f*), the helicity dissipation density h_d $(= -2\nu\boldsymbol{\omega} \cdot (\nabla \times \boldsymbol{\omega}))$ is typically negative where h is positive, and vice versa.

Figure 12(*a*) shows the time evolution of volume integration of H_d for different Re. Note that negative/positive values of H_d denote decreases/increases of H, respectively. Before reconnection ($t^* < 3.5$), H is transferred from writhe to twist helicity, which then decays due to dissipation; thus, H_d is slightly negative. During reconnection, H_d surges, and its rate of growth increases with Re. The time of the peak of H_d to occur decreases as Re increases, which is consistent with the earlier reconnection at higher Re. After reconnection, H_d becomes negative again for $Re = 2000$ but remains positive for the two high Re cases, which agrees with the increases of H. Interestingly, there is a distinct second peak around $t^* = 6.5$ for $Re = 12\,000$ – yet to be explained.

Figure 13(*a–c*) show the distribution of helicity density at several instants for $Re = 6000$ with figure 13(*d–f*) showing the corresponding helicity dissipation density h_d. Again, different from energy or enstrophy, helicity is not positive-sign definite. Hence, in the positive h region, negative h_d indicates helicity dissipation, while in the negative h region, positive h_d suggests helicity dissipation. First, as the knotted vortex propagates upward (along the z-direction), structures with negative helicity density appear in the reconnection region – suggesting that the anti-parallel structures are oppositely polarized (see figure 14(*a*) for a better view). As a consequence, the bridges formed during reconnection also become oppositely polarized between two legs (figure 14*b*,*c*), similar to that sketched by Melander & Hussain (1988) and Kida & Takaoka (1994) and observed by van Rees, Hussain & Koumoutsakos (2012) for reconnection of anti-parallel vortex tubes.

https://doi.org/10.1017/jfm.2021.580 Published online by Cambridge University Press

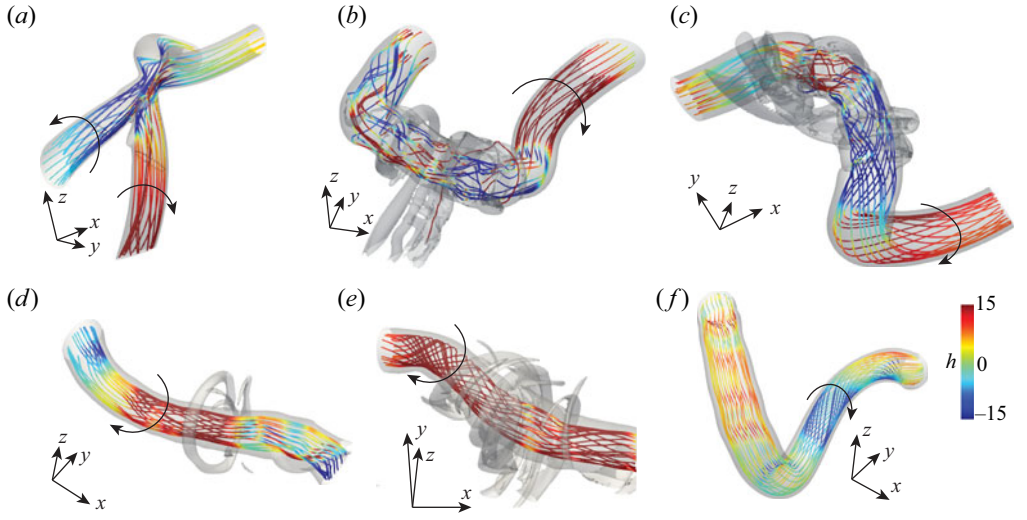


Figure 14. Vortex lines shaded with helicity density for structures I–VI marked in figure 13. The black arrow indicates the rotating direction of the vortex.

However, there is one important difference: for the anti-parallel cases considered by Melander & Hussain (1988) and others, reconnection is exactly symmetric, and the helicity density in the two legs have equal strengths; however, reconnection here is asymmetric, and, as we will show later, the helicity density in the two legs have unequal strengths. The negative helicity density dominates the positive for the bridge in SLR, while it reverses for the bridge in LTR. At late times (e.g. $t^* = 6.01$), negative h regions are mainly located in the threads that wrap around the rings (region IV–V in figure 13*c*) and the kinked part of the rings (region VI in figure 13*c*). Figure 13(*d–f*) show that the regions with strong h have strong h_d of opposite sign – indicating that large helicity dissipation occurs in strong helical region. However, it is rather difficult to tell from figure 13(*d–f*) whether the total dissipation H_d is positive or negative.

Figure 15 shows the isosurface of helicity density for $Re = 12\,000$. Due to reduced viscous diffusion, the structures look thinner than those at $Re = 6000$ (figure 13). Similar to that at $Re = 6000$, initially the negative h structures are mainly located in the anti-parallel reconnection region (figure 15*a*). Compared with that at $Re = 6000$, more negative h structures are observed after reconnection, especially in SLR (figures 15*b*). At a late time, these structures cascade into smaller scales. Besides, the rings are wrapped around with numerous threads, which are polarized due to flow induced by the rings – akin to that observed in vortex-turbulent interaction (Pradeep & Hussain 2010). In addition, the threads that connect SLR and LTR further undergo reconnection forming secondary bridges, similar to that observed in Yao & Hussain (2020*b*). However, compared with elsewhere, h there is negligible due to rapid dissipation caused by a rather small core size.

Although the global helicity is positive, as shown in figures 13 and 15, structures with strong negative h evolve during reconnection. In addition, the negative h structures increase with Re and can survive for a very long time after reconnection. To quantify that, figure 12(*b*) further shows the volume-integrated positive and negative helicity

https://doi.org/10.1017/jfm.2021.580 Published online by Cambridge University Press

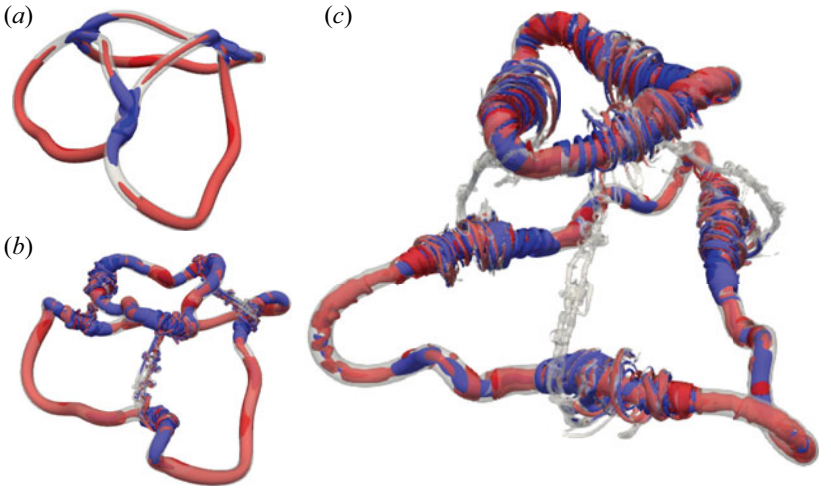


Figure 15. Isosurface of helicity density $h = \boldsymbol{u} \cdot \boldsymbol{\omega}$ for $Re = 12\,000$ at: (*a*) $t^* = 3.63$, (*b*) $t^* = 4.29$ and (*c*) $t^* = 6.01$. Note that the red and blue colours denote positive and negative 5 % of the maximum value, and the transparent (grey) isosurface represents $|\boldsymbol{\omega}| = 0.04\omega_0$.

$H^{\pm} = \int h^{\pm}\,\mathrm{d}V$, where

$$h^{+} = \begin{cases} h, & \text{if } h \geq 0, \\ 0, & \text{otherwise}, \end{cases} \tag{4.3}$$

and $h^{-} = h - h^{+}$. Note that a small non-zero value of H^{-} exists at an early time, presumably due to our specific initial condition (i.e. the three 'kinks' in the inner circle). As it rapidly decreases to zero due to viscous dissipation, it has a negligible effect on late evolution. It is interesting to observe that both H^{-} and H^{+} slowly grow during the initial stage when the knotted vortex starts to form anti-parallel structures. Just before reconnection, both of them rapidly increase at roughly the same rate; hence, H remains roughly conserved. This is somehow expected, as the helicity production H_p should produce zero net helicity ((4.2)). Consistent with H, the growth rate of $H^{\pm}$ increases with Re. After reconnection, the magnitudes of both H^{+} and H^{-} decrease, but non-monotonically. Surprisingly, at high Re, the decay rate for H^{-} is found to be larger than H^{+}. It implies that generation of twisted structures and the more rapid decay of those with negative h cause the net growth of H for $Re = 6000$ and 12 000.

4.3. *Mechanism for transient helicity growth*

Figure 16 shows the evolution of $\tilde{T}_w$ for the vortex knot before reconnection and for SLR and LTR and their sum after reconnection. Several comments deserve to be made. First, $\tilde{T}_w$ is equal to T_w at $t^* = 0$, or even before reconnection occurs. During and after reconnection, due to the presence of linked vortex lines, such as those in the threads, which connect two rings, and those in localized linked structures (figure 15), $\tilde{T}_w$, which also has some contributions from L_k, is no longer equivalent to T_w. As shown in figure 11, the increase of $\tilde{T}_w$ (and also T_w) before reconnection is mainly due to the growth of torsion T_t converted from writhe W_r. Note that although the net contribution of intrinsic twist T_i to $\tilde{T}_w$ is small, it does not mean that it is small everywhere. Instead, as discussed in Yao & Hussain (2021), the intrinsic twist helicity is mainly generated through an inviscid splitting mechanism,

https://doi.org/10.1017/jfm.2021.580 Published online by Cambridge University Press

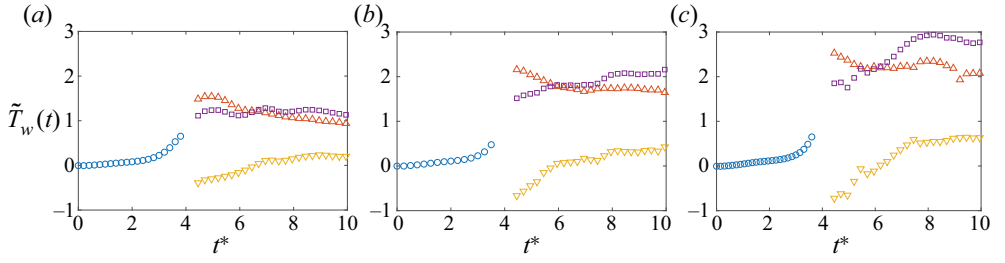


Figure 16. Time evolution of the generalized twist $\tilde{T}_w$ (calculated as $H/\Gamma^2 - W_r$) for the vortex knot before reconnection (circle), and for SLR (△), LTR (▽) and their sum (□): (*a*) $Re = 2000$, (*b*) 6000 and (*c*) 12 000.

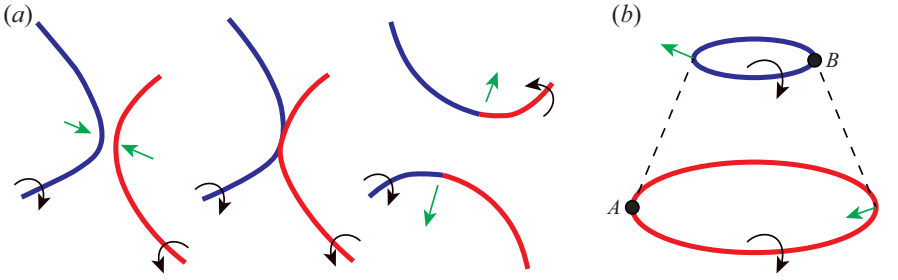


Figure 17. Schematic of (*a*) asymmetric reconnection of two vortex filaments with opposite sign of helicity density, and (*b*) mutual induction between two co-axial vortex rings. The black arrows denote the rotating direction of the vortex filaments, and the green arrows represent the induced velocity.

where structures with positive and negative intrinsic twist are generated simultaneously and equally (figures 13 and 15).

After reconnection, the total generalized twist $\tilde{T}_w$ slightly decreases for $Re = 2000$ but increases for the two high Re cases – consistent with the variation of the global helicity H (figure 3*b*). Since after reconnection the trefoil knot develops into two separate coiled vortex rings, their dynamics and interaction should explain the post-reconnection evolution of $\tilde{T}_w$ and H. In addition, the increase of total $\tilde{T}_w$, as well as H for high Re after reconnection is mainly due to the increase of $\tilde{T}_w$ in SLR. We find that just after reconnection, the LTR is overall positively twisted, while SLR is predominantly negatively twisted. It suggests that the newly generated helicity density h is unequally divided into small and large rings, with more negative h being transferred into the small ring. This unequal splitting of h is again mainly due to asymmetric reconnection, which is further illustrated in figure 17(*a*). Two vortex filaments with opposite signs of h collide and reconnect asymmetrically to form two new filaments, with one associated with predominant positive h and the other with negative h.

For the negatively twisted SLR, $\tilde{T}_w$ slowly decays due to viscous dissipation, causing the total helicity for SLR to increase (figure 10*a*). As Re increases, more negative h are generated before and during reconnection (figure 12*b*). Consequently, negative twist in SLR is enhanced after reconnection, which results in an increased dissipation of twist helicity, hence a rapid growth of $\tilde{T}_w$ – despite the fact that viscosity ν is reduced. Note that different from a single coiled ring (Scheeler *et al.* 2014), where $\tilde{T}_w$ eventually decays to zero, here $\tilde{T}_w$ of SLR alternate in sign and becomes positive at late time. The reason is that as SLR is stretched, part of the writhe helicity is converted to the twist helicity, similar to

https://doi.org/10.1017/jfm.2021.580 Published online by Cambridge University Press

that happening to the trefoil knot before reconnection. A LTR is initially associated with a positive net twist, which then continuously decreases due to viscous dissipation. Note that different from SLR, the decay rate of LTR decreases with Re, with is mainly attributed to smaller ν.

From figure 16, the different behaviours of twist and global helicity evolution at different Re are mainly due to differing twist decay rates for SLR and LTR. For a twisted rectilinear vortex column, the relative dissipation of twist depends mainly on core size σ and viscosity ν, i.e. $\partial T_w/\partial t = -2\nu T_w/\sigma^2$. However, for a coiled vortex ring, due to the presence of writhe and twist conversion, the dissipation may also be affected by its geometry, such as the ratio between core size and radius (σ/R) and the writhe. For example, Scheeler *et al.* (2017) showed that $\partial T_w/\partial t$ increases with σ/R for a three-coiled vortex ring. Furthermore, for the interacting coiled vortex rings considered here, the dissipation also depends on the influence of the other ring. The induced motion of LTR stretches the SLR (figure 17*b*), causing more rapid energy and helicity cascade to small scales (figures 15*c*); hence more dissipation. To account for these effects, we simply include a correction term g in the twist dissipation, which yields

$$\frac{\partial T_w}{\partial t} = -cgT_w, \tag{4.4}$$

where c represents $2\nu/\sigma^2$. As the geometries of SLR and LTR vary very mildly with Re, for simplicity, we further assume g is independent of Re. Accordingly, the twist for each ring follows

$$T_w = T_{w,0}\,\mathrm{e}^{-cgt}. \tag{4.5}$$

From figure 16 we have the following relationship regarding the initial twist in SLR ($T^s_{w,0}$) and LTR ($T^l_{w,0}$):

$$T^s_{w,0} < 0, \quad T^l_{w,0} > 0, \quad |T^s_{w,0}| < |T^l_{w,0}|. \tag{4.6a–c}$$

Therefore, the total twist can be expressed as

$$T_w = |T^l_w| - |T^s_w| = |T^l_{w,0}|e^{-cg^l t} - |T^s_{w,0}|e^{-cg^s t}. \tag{4.7}$$

Using the first-order Taylor expansion, we have

$$\begin{aligned} T_w &= |T^l_w| - |T^s_w| = |T^l_{w,0}|(1 - cg^l t) - |T^s_{w,0}|(1 - cg^s t) \\ &= \Delta T_{w,0} + \left(1 - \frac{g^l|T^l_{w,0}|}{g^s|T^s_{w,0}|}\right) cg^s|T^s_{w,0}|t, \end{aligned} \tag{4.8}$$

where $\Delta T_{w,0} = |T^l_{w,0}| - |T^s_{w,0}|$ is almost Re independent. From (4.8), the evolution of T_w mainly depends on the ratio between $g^l|T^l_{w,0}|$ and $g^s|T^s_{w,0}|$. As SLR is associated with a larger σ/R and is under stretching, it is expected to have $g^s > g^l$. At $Re = 2000$, the initial twist for LTR ($|T^l_{w,0}| \approx 1.5$) is much larger than that of SLR ($|T^s_{w,0}| \approx 0.5$). As a result, $(g^l|T^l_{w,0}|)/(g^s|T^s_{w,0}|) > 1$; hence, T_w decreases with time. However, the difference between $|T^l_{w,0}|$ and $|T^s_{w,0}|$ decreases as Re increases. In particular, $|T^l_w(0)|/|T^s_w(0)|$ becomes approximately 2 and 5/3 at $Re = 6000$ and 12 000. As a result, $(g^l|T^l_{w,0}|)/g^s|T^s_{w,0}| < 1$. Furthermore, at very high Re, $|T^l_w(0)|/|T^s_w(0)| \to 1$, and $(g^l|T^l_{w,0}|)/g^s|T^s_{w,0}|$ would approach g^l/g^s. Hence, T_w grows with time at high Re, and the rate of growth increases

https://doi.org/10.1017/jfm.2021.580 Published online by Cambridge University Press

with Re, which is consistent with those observed in figure 16. Note that both T_w^l and T_w^s would eventually decay to zero, as also does the total twist T_w.

In summary, although the twist in both SLR and LTR exponentially decay, the differences in their initial values and relative decay rates can result in a complex behaviour of the evolution of the total twist. In particular, it can lead to a transient growth of total twist as well as global helicity at high Re, which is analogous to the transient growth mechanism in stability theory (Schmid, Henningson & Jankowski 2002; Schoppa & Hussain 2002; Pradeep & Hussain 2010). In Appendix C we further demonstrate this by studying the evolution of two initially oppositely twisted vortex rings. Similar to previous studies (Mariani & Kontis 2010; Scheeler *et al.* 2017), the two vortex rings undergo leap-frogging. However, the total twist as well as global helicity can increase or decrease during different phases of leap-frogging – due to different decay rates of twist for each ring.

Note that the above explanation is based on the assumption that the dissipation follows a simple expression like (4.4). However, the actual dissipation rate is rather complicated. First, the distributions of vorticity and helicity in SLR and LTR are very irregular, especially at high Re (figures 13 and 15). Due to the mutual interaction of these two coiled rings, the twist helicity can grow or decay due to writhe to twist helicity conversion. In addition, the small-scale threads, which wrap around the rings, might also contribute to helicity dissipation, which we ignored. To better understand how geometry affects helicity dissipation and what the underlying mechanism is for the writhe and twist helicity conversion, configurations, such as the single coiled or interacting coiled vortex rings suggested by Scheeler *et al.* (2017), are desired.

4.4. *Helical wave decomposition*

To further elaborate the point that the generation of negative helical (or twist) structures and its faster decay in the SLR are the main cause for the transient growth of global helicity, we employ the helical wave decomposition to separate the total flow fields into purely right- and left-handed polarized structures. In Fourier space the velocity field can be split into two helical wave modes per wave vector

$$\hat{\boldsymbol{u}}(\boldsymbol{k}) = \hat{\boldsymbol{u}}^+(\boldsymbol{k}) + \hat{\boldsymbol{u}}^-(\boldsymbol{k}) = \hat{u}^+(\boldsymbol{k})\boldsymbol{h}^+(\boldsymbol{k}) + \hat{u}^-(\boldsymbol{k})\boldsymbol{h}^-(\boldsymbol{k}), \tag{4.9}$$

where $\boldsymbol{h}^\pm$ are the eigenvectors of the curl operator satisfying $\mathrm{i}\boldsymbol{k} \times \boldsymbol{h}^\pm = \pm|\boldsymbol{k}|\boldsymbol{h}^\pm$ and $u^\pm$ are the corresponding Fourier coefficients (Waleffe 1992; Lesieur 2012).

In real space the velocity field can be expressed in terms of complex helical waves and the gradient of a harmonic potential ϕ,

$$\boldsymbol{u}(\boldsymbol{x}) = \boldsymbol{u}^R(\boldsymbol{x}) + \boldsymbol{u}^L(\boldsymbol{x}) + \nabla\phi, \tag{4.10}$$

with $\boldsymbol{u}^R(\boldsymbol{x}) = \int \hat{\boldsymbol{u}}^+(\boldsymbol{k})\,\mathrm{d}\boldsymbol{k}$ and $\boldsymbol{u}^L(\boldsymbol{x}) = \int \hat{\boldsymbol{u}}^-(\boldsymbol{k})\,\mathrm{d}\boldsymbol{k}$. Note that $\boldsymbol{u}^R$ is the projection of $\boldsymbol{u}$ onto the vector space spanned by all eigenfunctions corresponding to positive eigenvalues $(+1|\boldsymbol{k}|)$ of the curl operator; hence, it is the so-called right-handed component of $\boldsymbol{u}$. Similarly, $\boldsymbol{u}^L$ is a linear combination of eigenfunctions corresponding to negative eigenvalues $(-1|\boldsymbol{k}|)$ and is the left-handed component of $\boldsymbol{u}$. In addition, for flow that is at rest at infinity, $\nabla\phi$ is a constant vector field and can be removed by choosing an appropriate inertial frame.

A similar decomposition can be applied to the vorticity field

$$\boldsymbol{\omega}(\boldsymbol{x}) = \boldsymbol{\omega}^R(\boldsymbol{x}) + \boldsymbol{\omega}^L(\boldsymbol{x}), \tag{4.11}$$

with $\boldsymbol{\omega}^R = \nabla \times \boldsymbol{u}^R$ and $\boldsymbol{\omega}^L = \nabla \times \boldsymbol{u}^L$.

https://doi.org/10.1017/jfm.2021.580 Published online by Cambridge University Press

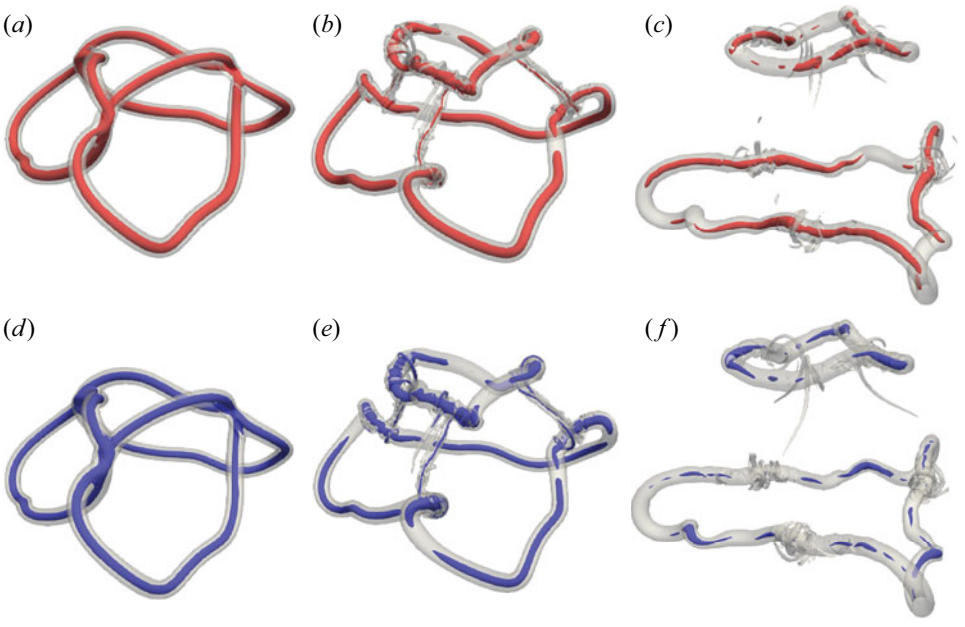


Figure 18. The right-handed (*a–c*) and left-handed (*d–f*) polarized components for vortical structures shown in figure 13: (*a*,*d*) $t^* = 3.74$, (*b*,*e*) $t^* = 4.29$ and (*c*,*f*) $t^* = 6.01$. Note that red and blue denotes positive and negative of 20 % of the maximum value of $h^{\pm}$; and the transparent (grey) isosurface represents $|\boldsymbol{\omega}| = 0.04\omega_0$.

Then, the helicity has a simple expression in terms of the decomposition

$$H = H^R + H^L = \int_V \boldsymbol{\omega}^R \cdot \boldsymbol{u}^R \,\mathrm{d}V + \int_V \boldsymbol{\omega}^L \cdot \boldsymbol{u}^L \,\mathrm{d}V. \tag{4.12}$$

Note that due to the orthogonality of the eigenfunctions of the curl operator, the contributions of cross-terms (i.e. $\boldsymbol{\omega}^L \cdot \boldsymbol{u}^R$ and $\boldsymbol{\omega}^R \cdot \boldsymbol{u}^L$) vanish. Different from H, H^R and H^L are positive and negative definite, respectively.

Helical wave decomposition has been mainly applied in statistical turbulence studies to examine the influence of helicity on the turbulent cascade (Waleffe 1993; Kessar *et al.* 2015). Differently, Melander & Hussain (1993) employed the decomposition in physical space to analyse flow fields as the dynamics of evolving polarized or helical structures. They found that a rectilinear vortex can be uniquely decomposed into right- and left-handed polarized components that travel in opposite directions, and the deformation of the total vortex column results primarily from the relative motion of these two structures, which evolve rather slow due to weakened interaction between modes in the same sign.

Figure 18 shows the right- and left-handed polarized components for structures in figure 13(*a–c*). It is clear that the original structures can be decomposed into structures with opposite polarization. Except for a slight difference in the threads, both of these structures resemble the original structures. The helicity density in both right- and left-hand polarized structures decays due to viscous dissipation, and at the late time, strong negative h are more localized at certain regions. In addition, although SLR is initially more left-handed polarized, the regions with negative h are more limited than those with a positive one at a late time – confirming our previous claim that the rapid decay of (negative) twist in SLR is the main reason for the increase of global helicity.

Figure 19(*a*) shows the evolution of enstrophy for the right- and left-handed components (Ω^R and Ω^L). Overall, both Ω^R and Ω^L have the same behaviour as the global enstrophy

https://doi.org/10.1017/jfm.2021.580 Published online by Cambridge University Press

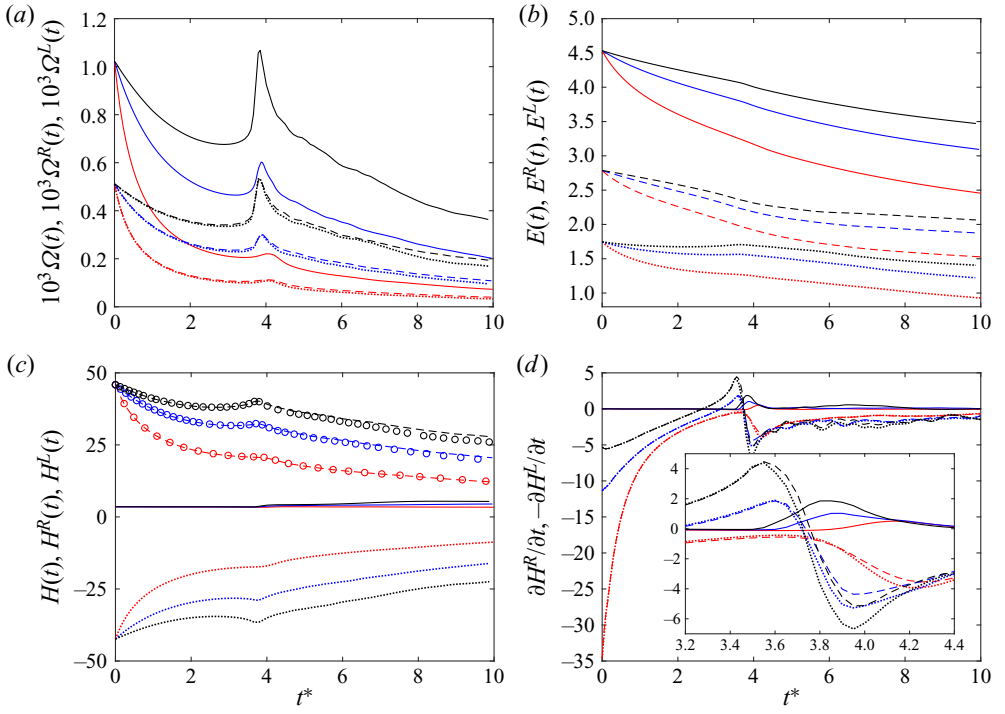


Figure 19. Time evolution of (*a*) enstrophy, (*b*) energy, (*c*) helicity and (*d*) rate of change of helicity for right-hand (dashed) and left-hand (dotted) polarized structures at $Re = 2000$ (red), 6000 (blue) and 12 000 (black). The global enstrophy, energy and helicity, which are the sum of right- and left-hand components, are shown in (*a–c*). Note that the circles in (*c*) denote $-H^L(t) + H(0)$, with $H(0) = 3.52$ the initial global helicity.

Ω: they decay initially and experience rapid growth during reconnection, followed by a rapid drop after reconnection. Initially, Ω^R and Ω^L have roughly the same magnitudes (approximately $\Omega/2$), but become different as time progresses. Besides, the disparity between Ω^R and Ω^L increases with Re – suggesting that the evolution of right- and left-handed polarized structures may become significantly different at sufficiently high Re. Figure 19(*b*) shows the evolution of energy for the total structures E and the right- and left-handed components (E^R and E^L). Due to viscous dissipation, the global energy $E(t)$ continuously decays, and the decay rate decreases with increasing Re. In addition, $E(t)$ decay faster during reconnection, which is due to the generations of small scales through intense stretching – consistent with a spike of $\Omega(t)$ in figure 19(*a*). Note that the energy (and also helicity) for purely right- and left-polarized components are not conserved in inviscid flows (Chen, Chen & Eyink 2003). Hence, E^R and E^L can decrease due to viscous dissipation or being transferred to the other. As the trefoil vortex knot is predominately right-hand polarized, $E^R(t)$ is larger than $E^L(t)$. While $E^R(t)$ continuously decreases similar to $E(t)$, the decay rate during reconnection is even faster than $E(t)$. It means that there is an energy transfer from the right-handed component to the left-handed one, which causes $E^L(t)$ for the two high Re cases to slightly increase during reconnection.

The helicity for right- and left-handed polarized components (H^R and H^L) as a function of t^* is displayed in figure 19(*c*). Note that due to the negative sign of H^L, the increase of H^L indicates the annihilation of the left-handed polarized structures. The evolution of H^R and H^L are much smoother compared with those of $H^\pm$ shown in

https://doi.org/10.1017/jfm.2021.580 Published online by Cambridge University Press

figure 12(*b*). It is interesting that $H^R(t)$ and $H^L(t)$ behave quite similar to those of Ω^R and Ω^L. Before reconnection, H^R (or H^L) exponentially decay (grow) due to viscous dissipation and slightly increase (decrease) during reconnection, and decay (grow) again after reconnection. However, the growth and decay rates are different between H^R and H^L, which results in complicated behaviours of H observed in figure 3. To further explore this point, figure 19(*d*) shows the rate of change of helicity for right- and left-handed components ($\partial H^R/\partial t$ and $-\partial H^R/\partial t$). Here, negative (positive) value denotes the diminish (enhance) of polarized structures. Consistent with the continuous decaying of H^R and growth of H^L for $Re = 2000$, $\partial H^R/\partial t$ and $-\partial H^L/\partial t$ remain negative all the time. For $Re = 6000$ and 12 000 cases, both $\partial H^R/\partial t$ and $-\partial H^L/\partial t$ increase and become positive before reconnection – consistent with the generation of polarized structures shown in figure 13(*a*). Besides, $\partial H^R/\partial t$ and $-\partial H^L/\partial t$ are almost identical before the first peak but become different as reconnection starts. In particular, $-\partial H^L/\partial t$ is slightly lower than $\partial H^R/\partial t$, which again suggests that the left-handed polarized structures decay faster than the right-handed ones – resulting in an increase of H. The difference between $-\partial H^L/\partial t$ and $\partial H^R/\partial t$ increases with increasing Re, which is consistent with a more rapid increase of H during reconnection at higher Re. After reconnection, the difference between $-\partial H^L/\partial t$ and $\partial H^R/\partial t$ slowly decreases for $Re = 2000$; but persists over a very long time for the two high Re cases. It confirms that the faster decay of left-handed polarized structures is the main cause of transient helicity growth at high Re.

4.5. *Energy and helicity spectra*

Figure 20(*a*,*c*,*e*) show the energy spectra at various instants for different Re cases. At $t^* = 0$, $E(k)$ falls smoothly at high wavenumbers owing to the Gaussian profile of the vorticity distribution. Due to viscous dissipation, $E(k)$ at small wavenumbers (i.e. $k \leq 50$) continuously decreases with time. However, at high wavenumbers a slight increase of $E(k)$ is observed for $t^* = 4.45$, which is due to the generation of small scales, such as threads, during reconnection. After reconnection, these small scales rapidly decay at $Re = 2000$ due to a strong viscous effect; hence, the energy at high wavenumbers quickly drops. An increase in Re results in generating additional smaller scales; thus, the increase of $E(k)$ at high wavenumbers is more pronounced for high Re cases. For $Re = 12\,000$, $E(k)$ develops a power law close to $k^{-7/3}$ – akin to that observed by van Rees *et al.* (2012) for anti-parallel reconnection of polarized vortex tubes. Furthermore, the energy drop becomes slower at higher Re due to suppressed energy dissipation.

The helicity spectra for the right-handed $H^R(k)$ and left-handed $-H^L(k)$ components based on helical wave decomposition are displayed in figure 20(*b*,*d*,*f*). Note that for the pure right- and left-handed vortices, we have $H^R(k) = kE^R(k)$ and $H^L(k) = -kE^L(k)$ (Biferale, Musacchio & Toschi 2012; Kessar *et al.* 2015). In addition, the Schwarz's inequality suggests that $|H(k)| \leq kE(k)$. Overall, the evolution of $H^R(k)$ and $-H^L(k)$ are quite similar to that of $E(k)$. As the flow is predominant right-handed polarized, $H^L(k)$ at $t^* = 0$ is slightly smaller than $-H^R(k)$ at low wavenumbers. Both $H^R(k)$ and $-H^L(k)$ have certain oscillations, which is consistent with that observed in Xiong & Yang (2020) for initially twisted vortex knots. During the evolution, both $H^R(k)$ and $-H^L(k)$ decay at low wavenumbers. But they are manifested at high wavenumbers during reconnection, which is consistent with the generation of twist helicity in figure 14. At a given time, the helicity contents at high wavenumbers increase with Re. In addition, $-H^L(k)$ is always smaller than $H^R(k)$ at small wavenumbers, but is almost identical to $H^R(k)$ at very high wavenumbers. It indicates that fine-scale structures have no preference for polarization – agreeing with

https://doi.org/10.1017/jfm.2021.580 Published online by Cambridge University Press

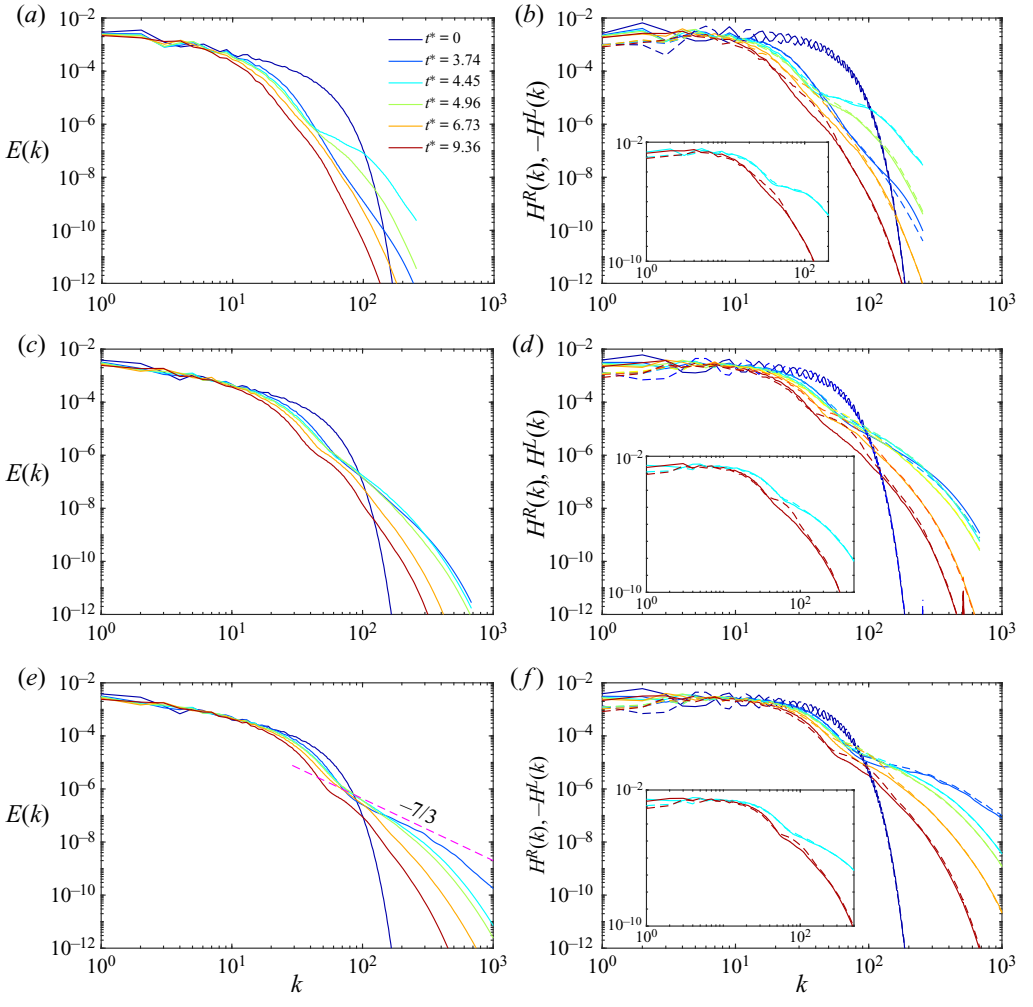


Figure 20. (*a*,*c*,*e*) Kinetic energy spectrum $E(k)$ of the total structures and (*b*,*d*,*f*) helicity spectrum for the right- and left-handed components at several instants for: (*a*,*b*) $Re = 2000$, (*c*,*d*) 6000 and (*e*,*f*) 12 000.

the conjecture by Brissaud *et al.* (1973) that helicity has a negligible dynamical effect at sufficiently high wavenumbers. However, it is interesting to note that at moderate wavenumbers (i.e. $k \approx 100$), $-H^L(k)$ is slightly larger than $H^R(k)$. This is consistent with more numerous small-scale negative h structures, mainly due to the stretching of SLR by LTR (figures 13*c* and 15*c*).

5. Effect of initial twist

We have shown that the generation of twist can cause the global helicity to grow after reconnection for high Re. In this section we further investigate the effect of twist on flow evolution via additional simulations of the trefoil vortex knotted with non-zero initial twist (i.e. $T_{w,0} = 7.48$ and 22.48). Figure 21 shows the time progression of flow structures visualized based on vorticity isosurface at $Re = 2000$ and 6000 for the $T_{w,0} = 22.48$ case. The flow evolution is quite similar to that for the $T_{w,0} = 0$ case, and the only apparent

https://doi.org/10.1017/jfm.2021.580 Published online by Cambridge University Press

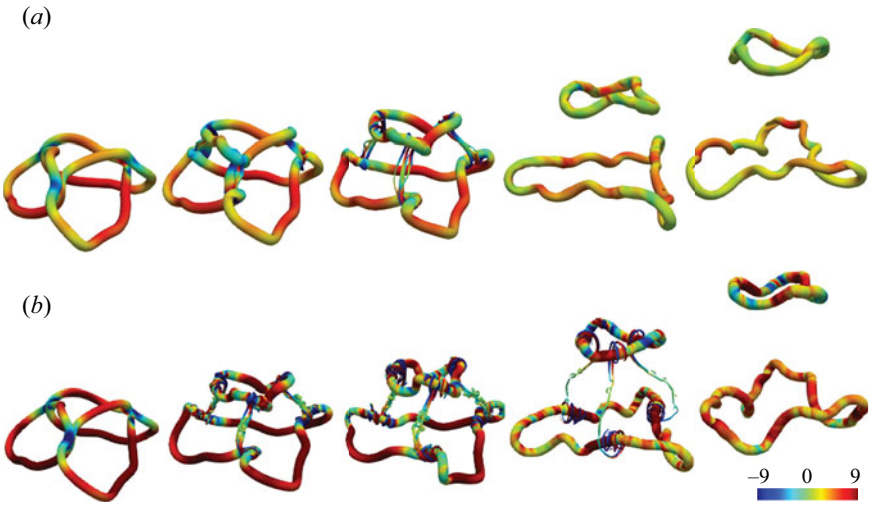


Figure 21. Evolution of flow structures represented by vorticity isosurface at 4 % of maximum initial vorticity (shaded in colour with helicity density) for (*a*) $Re = 2000$ and (*b*) $Re = 6000$ with $T_{w,0} = 22.48$.

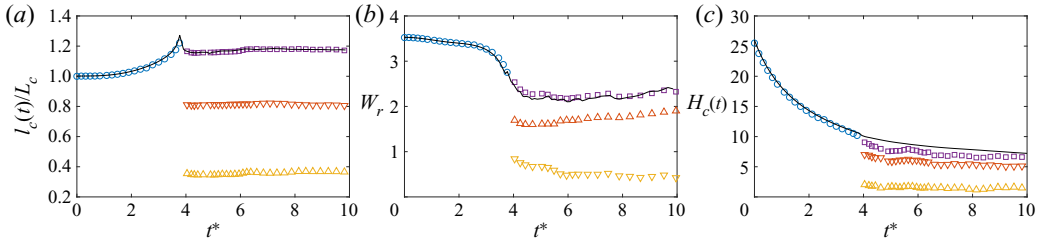


Figure 22. Time evolution of (*a*) the length l_c, (*b*) the writhe W_r and (*c*) the centreline helicity H_c of the vortex knot before reconnection (circle), and for SLR (△), LTR (▽) and their sum (□) for $Re = 6000$ with initial twist $T_{w,0} = 22.48$. Note that the solid lines in (*a*,*b*) are the total length and the helicity W_r for $Re = 6000$ with $T_{w,0} = 0$ cases, and in (*c*) are the global helicity H for $Re = 6000$ with $T_{w,0} = 22.48$.

difference is the distribution of the helicity density, which also becomes quite similar at late times due to the rapid decay of twist helicity. The similarity in flow evolution is further confirmed in figure 22(*a*,*b*) where the length and writhe of the vortex at $Re = 6000$ for the $T_{w,0} = 22.48$ case are almost identical to those of the $T_{w,0} = 0$ case. It suggests that compared with twist, the writhe plays a more important role in the evolution of knotted vortices. In addition, figure 22(*c*) shows that the centrelinehelicity H_c agrees with H before reconnection and becomes smaller than H after reconnection. But the difference between them decreases with time.

Figure 23(*a*) shows the evolution of enstrophy Ω (normalized by its initial value Ω_0) for different initial twist cases. Overall, the evolution is quite similar to that of the $T_{w,0} = 0$ cases. However, compared with the $T_{w,0} = 0$ cases, the enstrophy Ω decays faster as T_w increases. In Appendix B we demonstrate that, for a rectilinear Batchelor vortex column, the decay rate of Ω monotonously increases with the strength of twist. The faster decay of Ω is also consistent with the claim that helicity can inhibit energy transfer due to its role in depleting nonlinear interaction (Wu *et al.* 2007). Besides, the time for the peak of Ω to occur slightly increases as $T_{w,0}$ increases, which suggests that reconnection delays for

https://doi.org/10.1017/jfm.2021.580 Published online by Cambridge University Press

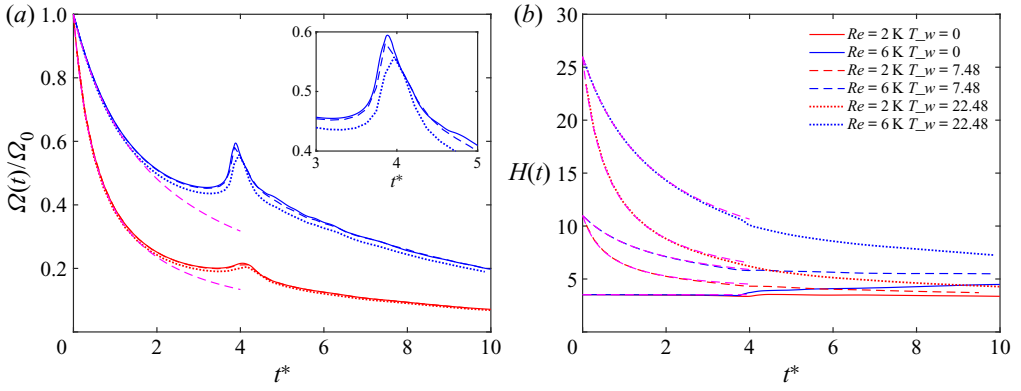


Figure 23. Time evolution of (*a*) the enstrophy Ω and (*b*) global helicity H for different initial twist and Reynolds numbers. The dashed lines in (*a*,*b*) denote $\Omega(t) = \Omega_0 \exp[-\int_0^t (2\nu/\sigma^2)]\,\mathrm{d}t$ and $H(t) = \Gamma^2 W_r(0) + \Gamma^2 T_w(0) \exp[-\int_0^t (2\nu/\sigma^2)\,\mathrm{d}t]$ with $\sigma = \sqrt{\sigma_0^2 + 2\nu t}$, respectively.

strong $T_{w,0}$ cases. It is consistent with the previous finding that the self-induced velocity of the vortex is reduced by increasing axial flows (Virk, Hussain & Kerr 1995; Cheng, Lou & Lim 2016).

The evolution of global helicity H for different initial twist cases is shown in figure 23(*b*). In contrast to the $T_{w,0} = 0$ cases, where H is mainly in the form of W_r and is almost constant initially, H rapidly decays for the $T_w \neq 0$ cases, and the decay rate increases with T_w. As discussed above, for a twisted straight vortex column, T_w is dissipated at a rate $(1/T_w)\partial t/\partial T_w = -2\nu/\sigma^2$ with $\sigma = \sqrt{\sigma_0^2 + 2\nu t}$. Hence, by assuming that writhe remains conserved, the helicity should roughly follow $H = \Gamma^2 W_r(0) + \Gamma^2 T_w(0) \exp[-\int_0^t (2\nu/\sigma^2)]\,\mathrm{d}t$. For all cases, the helicity evolution before reconnection agrees with the theoretical prediction based on the straight vortex. Different from the $T_{w,0} = 0$ cases, the rapid increase of H after reconnection is not observed. Instead, H continuously decays for all the time, but the decay rate decreases after reconnection.

Figures 24(*a*) further shows the volume-integrated positive and negative helicities $H^{\pm} = \int h^{\pm}\,\mathrm{d}V$ for $Re = 6000$ with $T_{w,0} = 22.48$. Initially, H^- is zero, indicating that all structures are associated with positive h. Similar to the $T_{w,0} = 0$ case, structures with negative h develop before reconnection; as a result, H^- starts to increase and reach a peak around the time of reconnection. But compared with the $T_{w,0} = 0$ case, H^- decreases for $T_{w,0} = 22.48$. The decrease of H^- for strong $T_{w,0}$ cases seems to be consistent with the suppression of the energy cascade. Figure 24(*b*) shows the evolution of enstrophy of the right- and left-handed components (Ω^R and Ω^L) for $Re = 6000$ with $T_{w,0} = 22.48$. Both Ω^R and Ω^L exhibit similar trends as those for the $T_{w,0} = 0$ case. Since the knotted vortex is strongly right polarized, Ω^R is initially much larger than Ω^L. In addition, Ω^R for the $T_{w,0} = 22.48$ case is always larger than that for the $T_{w,0} = 0$ case, but the difference continuously decreases with time. Similarly, Ω^L for the $T_{w,0} = 22.48$ case is always smaller than that for the $T_{w,0} = 0$ case, and the difference decreases with time. Thus, although the vortices are initialized with different twists, the flow would eventually become identical. Figure 24(*c*) further compares the total energy and energy of the right- and left-handed components between the $T_{w,0} = 0$ and 22.48 cases. Despite a distinct difference of Ω between these two cases, the evolution of $E(t)$ is visually identical.

https://doi.org/10.1017/jfm.2021.580 Published online by Cambridge University Press

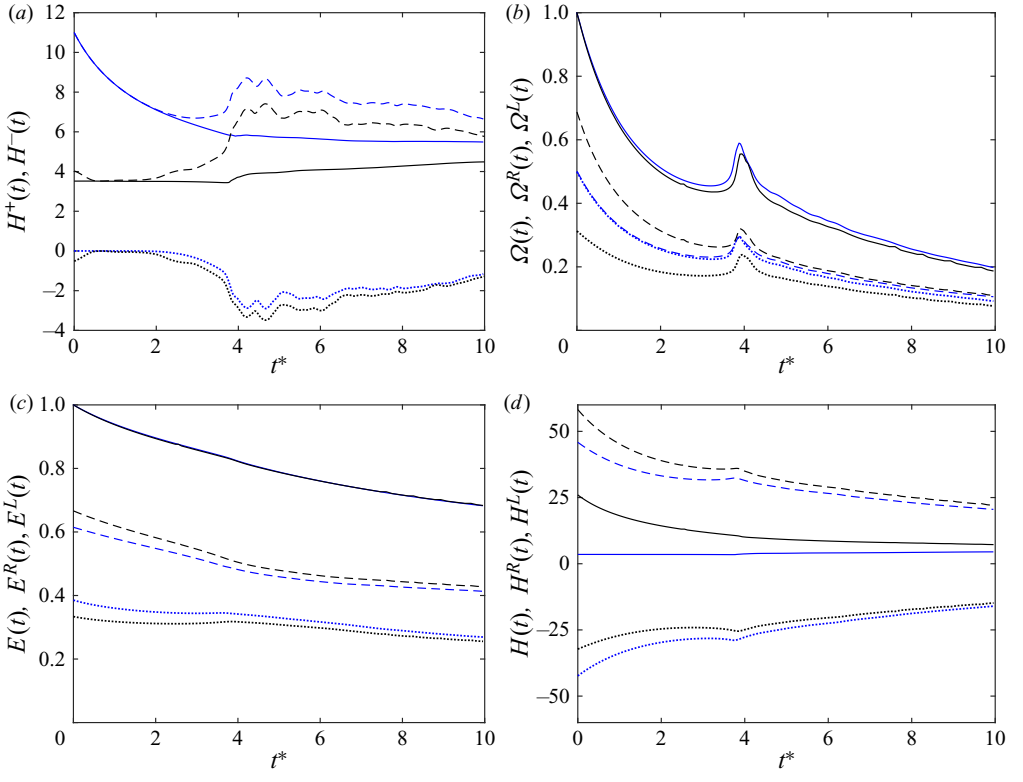


Figure 24. Time evolution of (*a*) $H^{\pm}$, (*b*) enstrophy, (*c*) energy and (*d*) helicity for $Re = 6000$ with $T_{w,0} = 0$ (black) and $T_{w,0} = 22.48$ (blue). The solid, dashed and dotted lines in (*a*) denote H, H^+ and H^-, respectively, and in (*b–d*) represent quantities for global, right-handed and left-handed components.

Similar to that of enstrophy, $E^R(t)$ is much larger than $E^L(t)$ initially, and both of them slowly approach the values of the $T_{w,0} = 0$ case. From figure 24(*d*), it is clear that introducing twist enhances H^R and suppresses H^L simultaneously – suggesting that the flow becomes more Beltramized (i.e. $\boldsymbol{u} \| \boldsymbol{\omega}$). Due to its initial high value, H^R decays faster than H^L, causing a rapid decrease of H. During reconnection, although both H^R and H^L increase, the increase of H^R is slightly smaller than H^L – causing H to decrease. After reconnection, H^R and H^L decrease again and approach those of the $T_{w,0} = 0$ case.

Figure 25(*a*) shows the energy spectra at various instants for $Re = 6000$ with $T_{w,0} = 22.48$. The spectrum at $t^* = 0$ has slight oscillations at high wavenumbers, similar to those observed for the right-handed components of the $T_{w,0} = 0$ case (figure 20*b*). The evolution of $E(k)$ is almost identical to that of $T_{w,0} = 0$ case, consistent with the identical energy evolution of these two cases. The helicity spectra of the right- and left-handed components for $Re = 6000$ with $T_{w,0} = 22.48$ are shown in figure 25(*b*). For all k, $-H^L(k)$ is initially smaller than $H^R(k)$. As time progresses, the difference between $-H^L(k)$ and $H^R(k)$ at small k persists but decreases at high k. Consistent with the $T_{w,0} = 0$ case, $-H^L(k)$ is larger than $H^R(k)$ at moderate k.

https://doi.org/10.1017/jfm.2021.580 Published online by Cambridge University Press

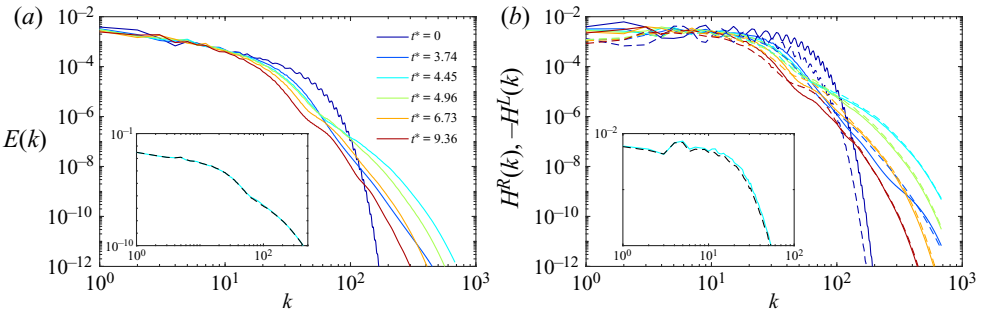


Figure 25. (*a*) Kinetic energy spectrum $E(k)$ of the total structures and (*b*) helicity spectrum for the right- and left-handed components at several instants for $Re = 6000$ and $T_{w,0} = 22.48$ case. The insets in (*a*,*b*) show the comparison of $E(k)$ and $H^R(k)$ at $t^* = 4.45$ between $T_{w,0} = 0$ (solid) and $T_{w,0} = 22.48$ (dashed) cases, respectively.

6. Concluding remarks

We performed direct numeral simulations of trefoil knotted vortices with different initial twists. Different from previous works (Scheeler *et al.* 2014; Kerr 2018*c*), we observed that the global helicity H is not conserved for the zero initial twist cases. It slightly decreases before reconnection; and its evolution after reconnection strongly depends on Re: for the low Re case, it slightly increases after reconnection, while for the high Re case, it remarkably increases for a long time before finally decaying – suggesting that helicity is not conserved during viscous reconnection (even at very higher Re). The centreline helicity, calculated as $H_c = \sum_i \Gamma_i \oint_{\mathcal{C}_i} \boldsymbol{u} \cdot \boldsymbol{T}(s)\,\mathrm{d}s$, is found to be a good approximation for H before and a long time after reconnection. In addition, the writhe W_r continuously decreases before reconnection and becomes preserved after reconnection, akin to that found in quantum reconnection (Scheeler *et al.* 2014). Different from the global helicity, the evolution of W_r is almost Re independent – suggesting that the strong twist helicity is generated at high Re.

Further analyses, such as flow visualization, helicity decomposition and helical wave decomposition, shows that significant amounts of positive and negative twist helicities are generated before and during reconnection. As the reconnection is asymmetric, the small leading and large trailing rings generated after reconnection are predominately negatively and positively twisted, respectively. Different from the straight vortex column, where the dissipation of twist $\partial T_w/\partial t$ depends on viscosity, initial twist value and core size, the rate of twist dissipation for a coiled vortex ring also depends on the geometry, particularly the core size to radius ratio. Besides, $\partial T_w/\partial t$ is also influenced by mutual induction of the other ring. Due to the relatively large value of the initial twist, $\partial T_w/\partial t$ for LTR is larger than that in SLR at $Re = 2000$ – resulting in a decrease of the total twist as well as global helicity. However, as Re increases, the difference between initial twist decreases, $\partial T_w/\partial t$ for SLT becomes larger than that for LTR – causing a 'transient' net increase of H at high Re.

In addition, reconnection of trefoil knotted vortices with different initial twist cases are considered. The flow structure evolution is quite similar to that of the zero initial twist case. In particular, the total length and the writhe are almost identical for different $T_{w,0}$ cases. One apparent difference is that the enstrophy and the associated energy dissipation are suppressed for strong $T_{w,0}$ cases. The suppressed energy cascade is found to be associated with decreased generation of the left-handed polarized structures. The results suggest that

https://doi.org/10.1017/jfm.2021.580 Published online by Cambridge University Press

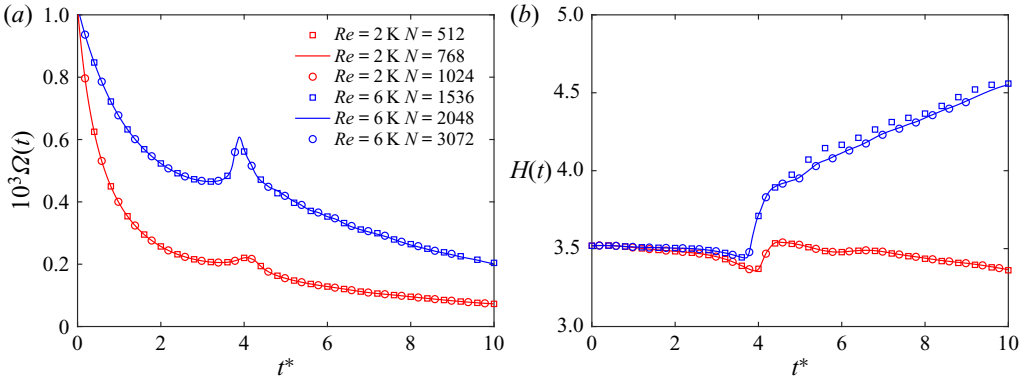


Figure 26. Time evolution of (*a*) enstrophy Ω and (*b*) global helicity H for $Re = 2000$ (red), 6000 (blue) with different grid resolutions.

although the writhe governs the evolution of knotted vortices, twist also plays an important role in flow dynamics, especially energy cascade and dissipation. In addition, the twist dissipation is strongly affected by the vortex core size. It would be interesting to investigate the effects of the radius of knots and core size on the reconnection dynamics. In addition, studies of single and interacting coiled vortex rings are required to better understand the mechanism of writhe and twist conversions.

Acknowledgements. Computational and visualization resources provided by Texas Tech University HPCC, TACC Lonestar, Frontera and Stampede2 under XSEDE are acknowledged.

Declaration of interests. The authors report no conflict of interest.

Author ORCIDs.
Jie Yao https://orcid.org/0000-0001-6069-6570;
Yue Yang https://orcid.org/0000-0001-9969-7431;
Fazle Hussain https://orcid.org/0000-0002-2209-9270.

Appendix A. Grid convergence analysis for $Re = 2000$ and 6000

A grid sensitivity analysis has been carried out for Reynolds numbers $Re = 2000$ and 6000. For each Re, three different grid resolutions are tested, namely, $N^3 = 512^3$, 768^3 and 1024^3 for $Re = 2000$; and $N^3 = 1536^3$, 2048^3 and 3072^3 for $Re = 6000$. Figure 26(*a*) shows the time evolution of enstrophy Ω for the three different grid resolutions at $Re = 2000$ and 6000. As Ω is very sensitive to small-scale dynamics, the collapse of Ω indicates that the resolutions we employed in the main text are sufficient to capture the small scales generated during the reconnection process. The evolution of the global helicity H is shown in figure 26(*b*), where good agreements among different resolutions are also observed. Note that the small difference for the $Re = 6000$ and $N^3 = 1536^3$ case after reconnection might be due to its insufficiency in capturing the axial velocity associated with the twist structures in the rings.

Appendix B. Enstrophy and helicity dissipation for a Batchelor vortex

Consider a straight Batchelor vortex (figure 27); its vorticity distribution is $\boldsymbol{\omega} = [\omega_r, \omega_\theta, \omega_z] = [0, rqf, f]$, where q quantifies the strength of the axial flow and f is the

https://doi.org/10.1017/jfm.2021.580 Published online by Cambridge University Press

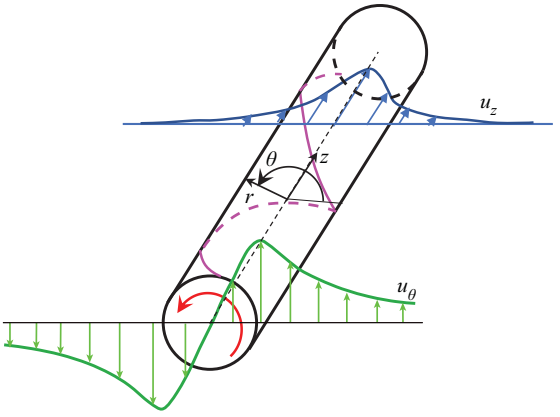


Figure 27. Schematic illustration of the Batchelor vortex. Note that the red arrow represents the rotation direction of the vortex, and the purple line denotes the vortex lines.

axial vorticity distribution given in (2.10). The enstrophy dissipation rate is given as

$$\frac{\partial \Omega}{\partial t} = -\nu \int (\nabla \boldsymbol{\omega})^2 \,\mathrm{d}V = \nu \int [(\omega_\theta/r)^2 + (\partial \omega_\theta/\partial r)^2 + (\partial \omega_z/\partial r)^2] \,\mathrm{d}V \tag{B1}$$

$$= \nu \int [2q^2 f^2 + (1 + r^2 q^2) f'^2 + 2rq^2 f f'] \,\mathrm{d}V, \tag{B2}$$

which can be simplified as a relative decay rate

$$\frac{\partial \Omega}{\partial t} = -2\nu\Omega \frac{2q^2\sigma^2 + 1}{(q^2\sigma^2 + 1)\sigma^2}. \tag{B3}$$

Here σ is the vortex core scale and grows as $\sigma(t) = \sqrt{\sigma_0^2 + 2\nu t}$ in a viscous flow. Note that the decay rate is $-2\nu\Omega/\sigma^2$ for the special $q = 0$ case (Lamb–Oseen vortices), and asymptotically increases as q increases. The rapid decay for the strong q case is consistent with the claim that the helicity can suppress energy dissipation as $\epsilon = \nu\Omega$.

Similarly, the helicity dissipation rate is

$$\frac{\partial H}{\partial t} = -2\nu \int \boldsymbol{\omega} \cdot (\nabla \times \boldsymbol{\omega}) \,\mathrm{d}V = -4\nu q \int f^2 \,\mathrm{d}V = -2\nu H/\sigma^2. \tag{B4}$$

This dissipation depends on viscosity and core size. As the helicity is in the form of twist only, this is equivalent to a dissipation of the total twist ($\partial T_w/\partial t = -2\nu T_w/\sigma^2$).

Appendix C. Helicity evolution for two co-axial oppositely twisted vortex rings

We consider the dynamics of two co-axial oppositely twisted vortex rings undergoing a leap-frogging motion. The radii of inner and outer rings are $R_i = 0.5$ and $R_o = 1$, respectively, and the circulation and the core size are the same as for the trefoil knot (i.e. $\Gamma = 1$ and $\sigma = 1/(16\sqrt{2\pi}) \approx 0.025$). The initial inner and outer rings are negatively and positively twisted, respectively, with the correspondingly initial twists $T^i_{w,0} = -9$ and $T^o_{w,0} = 10$. The simulation is performed at $Re = 6000$ with grid points $N^3 = 768^3$.

Figure 28 shows the evolution of global helicity along with the vortices visualized based on the isosurface of $|\boldsymbol{\omega}|$. Note that as the writhe remains zero, the global helicity

https://doi.org/10.1017/jfm.2021.580 Published online by Cambridge University Press

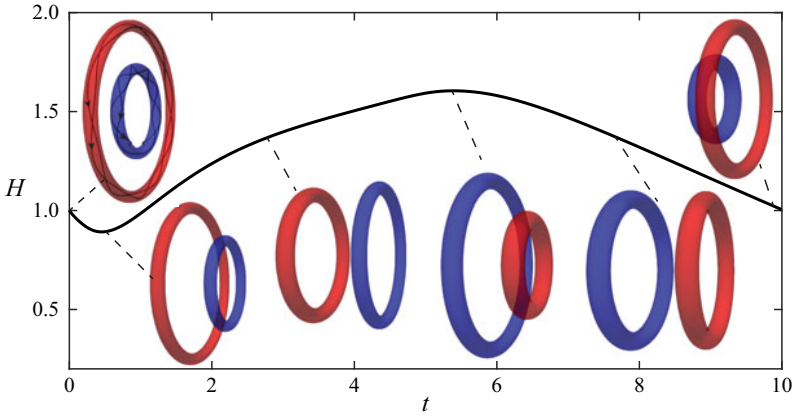


Figure 28. Time evolution of the global helicity H for the co-axial oppositely twisted vortex rings. Flow structures are represented by vorticity isosurface at 4 % of maximum initial vorticity shaded with positive (red) and negative (blue) helicity densities.

$H = \Gamma^2 T_w = \Gamma^2 (T_w^i + T_w^o)$. Here T_w^i and T_w^o denote the twist for the inner and outer rings, respectively. Following Appendix B, the dissipation rate of each ring is $\partial T_w/\partial t = -2\nu T_w/\sigma^2(t)$, with $\sigma(t)$ denoting the core size. The two rings remain isolated during the evolution; hence, the circulation Γ for each ring remains almost constant. Consequently, the dissipation rate of H is

$$\frac{\partial H}{\partial t} = -2\nu\Gamma^2 \left(\frac{T_w^i}{\sigma_i^2(t)} + \frac{T_w^o}{\sigma_o^2(t)} \right), \tag{C1}$$

which suggest that H can either increase or decrease, depending on the relative value between T_w^i/σ_i^2 and T_w^o/σ_o^2.

Initially, as two rings are in the same plane, stretching and compression are limited; hence, the core sizes of the rings are almost unchanged. Although the twist in both rings decays, the helicity decreases as the (positive) twist of the outer ring decays faster due to its larger initial value. However, when the inner ring advects sufficient far away from the outer ring, the inner and outer rings, respectively, undergo stretching and compression (as sketched in figure 17*b*). As a result, the core sizes of the inner and outer ring become smaller and larger, respectively; hence, the (negative) twist in the inner ring decays faster; therefore, the global helicity starts to grow. This is similar to the increase of twist and helicity for trefoil knot after reconnection, as shown in figure 3 and implied by (4.8). In the process of leap-frogging, the total twist and global helicity can sometimes increase or decrease, as the two rings have different decay rates based on whether they are compressed or stretched. Note that the interaction between SLR and LTR after trefoil knot reconnection is much more complicated than what we consider here. As these two rings are coiled, there are additional conversions between the writhe and twist helicity during successive compression or stretching of the two rings.

References

Alamri, S.Z., Youd, A.J. & Barenghi, C.F. 2008 Reconnection of superfluid vortex bundles. *Phys. Rev. Lett.* **101** (21), 215302.

Archer, P.J., Thomas, T.G. & Coleman, G.N. 2008 Direct numerical simulation of vortex ring evolution from the laminar to the early turbulent regime. *J. Fluid Mech.* **598**, 201–226.

https://doi.org/10.1017/jfm.2021.580 Published online by Cambridge University Press

ASHURST, W.T. & MEIRON, D.I. 1987 Numerical study of vortex reconnection. *Phys. Rev. Lett.* **58** (16), 1632.
BAGGALEY, A.W. & BARENGHI, C.F. 2011 Spectrum of turbulent kelvin-waves cascade in superfluid helium. *Phys. Rev.* B **83** (13), 134509.
BATCHELOR, G.K. 2000 *An Introduction to Fluid Dynamics*. Cambridge University Press.
BEWLEY, G.P., PAOLETTI, M.S., SREENIVASAN, K.R. & LATHROP, D.P. 2008 Characterization of reconnecting vortices in superfluid helium. *Proc. Natl Acad. Sci.* **105** (37), 13707–13710.
BIFERALE, L., MUSACCHIO, S. & TOSCHI, F. 2012 Inverse energy cascade in three-dimensional isotropic turbulence. *Phys. Rev. Lett.* **108** (16), 164501.
BORATAV, O.N., PELZ, R.B. & ZABUSKY, N.J. 1992 Reconnection in orthogonally interacting vortex tubes: direct numerical simulations and quantifications. *Phys. Fluids* A **4** (3), 581–605.
BRETHERTON, F.P. 1970 A note on Hamilton's principle for perfect fluids. *J. Fluid Mech.* **44** (1), 19–31.
BRISSAUD, A., FRISCH, U., LEORAT, J., LESIEUR, M. & MAZURE, A. 1973 Helicity cascades in fully developed isotropic turbulence. *Phys. Fluids* **16** (8), 1366–1367.
CANUTO, C., HUSSAINI, M.Y., QUARTERONI, A. & ZHANG, T.J. 2012 *Spectral Methods in Fluid Dynamics*. Springer Science & Business Media.
CHATELAIN, P., KIVOTIDES, D. & LEONARD, A. 2003 Reconnection of colliding vortex rings. *Phys. Rev. Lett.* **90** (5), 054501.
CHEN, Q., CHEN, S. & EYINK, G.L. 2003 The joint cascade of energy and helicity in three-dimensional turbulence. *Phys. Fluids* **15** (2), 361–374.
CHENG, M., LOU, J. & LIM, T.T. 2016 Evolution of an elliptic vortex ring in a viscous fluid. *Phys. Fluids* **28** (3), 037104.
DARYAN, H., HUSSAIN, F. & HICKEY, J.-P. 2020 Aeroacoustic noise generation due to vortex reconnection. *Phys. Rev. Fluids* **5**, 062702.
DYSON, F.W. 1893 The potential of an anchor ring. Part II. *Phil. Trans. R. Soc. Lond* A **184**, 1041–1106.
FONDA, E., MEICHLE, D.P., OUELLETTE, N.T., HORMOZ, S. & LATHROP, D.P. 2014 Direct observation of kelvin waves excited by quantized vortex reconnection. *Proc. Natl Acad. Sci.* **111**, 4707–4710.
FONDA, E., SREENIVASAN, K.R. & LATHROP, D.P. 2019 Reconnection scaling in quantum fluids. *Proc. Natl Acad. Sci.* **116** (6), 1924–1928.
GALANTUCCI, L., BAGGALEY, A.W., PARKER, N.G. & BARENGHI, C.F. 2019 Crossover from interaction to driven regimes in quantum vortex reconnections. *Proc. Natl Acad. Sci.* **116** (25), 12204–12211.
HIDE, R. 1989 Superhelicity, helicity and potential vorticity. *Geophys. Astrophys. Fluid Dyn.* **48** (1–3), 69–79.
HUSSAIN, A.K.M.F. 1986 Coherent structures and turbulence. *J. Fluid Mech.* **173**, 303–356.
HUSSAIN, F. & DURAISAMY, K. 2011 Mechanics of viscous vortex reconnection. *Phys. Fluids* **23** (2), 021701.
IYER, K.P., SREENIVASAN, K.R. & YEUNG, P.K. 2017 Reynolds number scaling of velocity increments in isotropic turbulence. *Phys. Rev.* E **95**, 021101.
JAQUE, R.S. & FUENTES, O.V. 2017 Reconnection of orthogonal cylindrical vortices. *Eur. J. Mech. (B/Fluids)* **62**, 51–56.
KERR, R.M. 2013 Swirling, turbulent vortex rings formed from a chain reaction of reconnection events. *Phys. Fluids* **25** (6), 065101.
KERR, R.M. 2018*a* Enstrophy and circulation scaling for Navier–Stokes reconnection. *J. Fluid Mech.* **839**, R2.
KERR, R.M. 2018*b* Topology of interacting coiled vortex rings. *J. Fluid Mech.* **854**, R2.
KERR, R.M. 2018*c* Trefoil knot timescales for reconnection and helicity. *Fluid Dyn. Res.* **50** (1), 011422.
KESSAR, M., PLUNIAN, F., STEPANOV, R. & BALARAC, G. 2015 Non-kolmogorov cascade of helicity-driven turbulence. *Phys. Rev.* E **92** (3), 031004.
KIDA, S. & TAKAOKA, M. 1987 Bridging in vortex reconnection. *Phys. Fluids* **30** (10), 2911–2914.
KIDA, S. & TAKAOKA, M. 1988 Reconnection of vortex tubes. *Fluid Dyn. Res.* **3** (1–4), 257–261.
KIDA, S. & TAKAOKA, M. 1994 Vortex reconnection. *Annu. Rev. Fluid Mech.* **26** (1), 169–177.
KIDA, S., TAKAOKA, M. & HUSSAIN, F. 1991 Collision of two vortex rings. *J. Fluid Mech.* **230**, 583–646.
KIMURA, Y. & MOFFATT, H.K. 2017 Scaling properties towards vortex reconnection under Biot–Savart evolution. *Fluid Dyn. Res.* **50** (1), 011409.
KIVOTIDES, D., VASSILICOS, J.C., SAMUELS, D.C. & BARENGHI, C.F. 2001 Kelvin waves cascade in superfluid turbulence. *Phys. Rev. Lett.* **86** (14), 3080.
KLECKNER, D. & IRVINE, W.T. 2013 Creation and dynamics of knotted vortices. *Nat. Phys.* **9** (4), 253–258.
KOPLIK, J. & LEVINE, H. 1993 Vortex reconnection in superfluid helium. *Phys. Rev. Lett.* **71** (9), 1375.
LAING, C.E., RICCA, R.L. & SUMNERS, D.W. 2015 Conservation of writhe helicity under anti-parallel reconnection. *Sci. Rep.* **5**, 9224.
LEE, M. & MOSER, R.D. 2015 Direct numerical simulation of turbulent channel flow up to Re 5200. *J. Fluid Mech.* **774**, 395–415.
LESIEUR, M. 2012 *Turbulence in Fluids*. Springer Science & Business Media.

https://doi.org/10.1017/jfm.2021.580 Published online by Cambridge University Press

LEVY, Y., DEGANI, D. & SEGINER, A. 1990 Graphical visualization of vortical flows by means of helicity. *AIAA J.* **28** (8), 1347–1352.
MAGGIONI, F., ALAMRI, S., BARENGHI, C.F. & RICCA, R.L. 2010 Velocity, energy, and helicity of vortex knots and unknots. *Phys. Rev.* E **82** (2), 026309.
MARIANI, R. & KONTIS, K. 2010 Experimental studies on coaxial vortex loops. *Phys. Fluids* **22** (12), 126102.
MCKEOWN, R., MONICO, R.O., PUMIR, A., BRENNER, M.P. & RUBINSTEIN, S.M. 2018 Cascade leading to the emergence of small structures in vortex ring collisions. *Phys. Rev. Fluids* **3** (12), 124702.
MELANDER, M.V. & HUSSAIN, F. 1988 Cut-and-connect of two antiparallel vortex tubes. In *Studying Turbulence Using Numerical Simulation Databases*, vol. 2, pp. 257–286. Center for Turbulence Research.
MELANDER, M.V. & HUSSAIN, F. 1993 Polarized vorticity dynamics on a vortex column. *Phys. Fluids* A **5** (8), 1992–2003.
MELANDER, M.V. & HUSSAIN, F. 1994 Core dynamics on a vortex column. *Fluid Dyn. Res.* **13** (1), 1–37.
MELANDER, M.V. & ZABUSKY, N.J. 1988 Interaction and "apparent" reconnection of 3D vortex tubes via direct numerical simulations. *Fluid Dyn. Res.* **3** (1–4), 247–250.
MOFFATT, H.K. 1969 The degree of knottedness of tangled vortex lines. *J. Fluid Mech.* **35** (1), 117–129.
MOFFATT, H.K. & RICCA, R.L. 1992 Helicity and the Călugăreanu invariant. *Proc. R. Soc. Lond.* A **439**, 411–429.
OBERTI, C. & RICCA, R.L. 2019 Influence of winding number on vortex knots dynamics. *Sci. Rep.* **9** (1), 17284.
ORLANDI, P., PIROZZOLI, S. & CARNEVALE, G.F. 2012 Vortex events in euler and Navier–Stokes simulations with smooth initial conditions. *J. Fluid Mech.* **690**, 288–320.
POHL, W.F. 1968 The self-linking number of a closed space curve. *J. Math. Mech.* **17**, 975–985.
PRADEEP, D.S. & HUSSAIN, F. 2004 Effects of boundary condition in numerical simulations of vortex dynamics. *J. Fluid Mech.* **516**, 115–124.
PRADEEP, D.S. & HUSSAIN, F. 2010 Vortex dynamics of turbulence–coherent structure interaction. *Theor. Comput. Fluid Dyn.* **24** (1–4), 265–282.
PRIEST, E. & FORBES, T. 2000 *Magnetic Reconnection: MHD Theory and Applications*. Cambridge University Press.
PROMENT, D. & KRSTULOVIC, G. 2020 A matching theory to characterize sound emission during vortex reconnection in quantum fluids. *Phys. Rev. Fluids* **5**, 104701.
PUMIR, A. & KERR, R.M. 1987 Numerical simulation of interacting vortex tubes. *Phys. Rev. Lett.* **58** (16), 1636.
VAN REES, W.M., HUSSAIN, F. & KOUMOUTSAKOS, P. 2012 Vortex tube reconnection at $Re = 104$. *Phys. Fluids* **24** (7), 075105.
SADLO, F., HAUSNER, P., HOFMANN, L., JUNG, P., KARCH, G., PEIKERT, R., PILZ, L., ROTH, M. & SDEO, K. 2019 VCG ParaView plugins.
SCHEELER, M.W., KLECKNER, D., PROMENT, D., KINDLMANN, G.L. & IRVINE, W.T. 2014 Helicity conservation by flow across scales in reconnecting vortex links and knots. *Proc. Natl Acad. Sci.* **111** (43), 15350–15355.
SCHEELER, M.W., VAN REES, W.M., KEDIA, H., KLECKNER, D. & IRVINE, W.T. 2017 Complete measurement of helicity and its dynamics in vortex tubes. *Science* **357** (6350), 487–491.
SCHMID, P.J., HENNINGSON, D.S. & JANKOWSKI, D.F. 2002 Stability and transition in shear flows. Applied Mathematical Sciences, vol. 142. *Appl. Mech. Rev.* **55** (3), B57–B59.
SCHOPPA, W. & HUSSAIN, F. 2002 Coherent structure generation in near-wall turbulence. *J. Fluid Mech.* **453**, 57–108.
SHELLEY, M.J., MEIRON, D.I. & ORSZAG, S.A. 1993 Dynamical aspects of vortex reconnection of perturbed anti-parallel vortex tubes. *J. Fluid Mech.* **246**, 613–652.
SIGGIA, E.D. 1985 Collapse and amplification of a vortex filament. *Phys. Fluids* **28** (3), 794–805.
SUJUDI, D. & HAIMES, R. 1995 Identification of swirling flow in 3-d vector fields. In *12th Computational Fluid Dynamics Conference*, p. 1715. The American Institute of Aeronautics and Astronautics.
TIAN, S., GAO, Y., DONG, X. & LIU, C. 2018 Definitions of vortex vector and vortex. *J. Fluid Mech.* **849**, 312–339.
VAZQUEZ, M. & SUMNERS, D.W. 2004 Tangle analysis of gin site-specific recombination. *Math. Proc. Camb. Phil. Soc.* **136**, 565–582.
VILLOIS, A., PROMENT, D. & KRSTULOVIC, G. 2017 Universal and nonuniversal aspects of vortex reconnections in superfluids. *Phys. Rev. Fluids* **2** (4), 044701.
VIRK, D., HUSSAIN, F. & KERR, R.M. 1995 Compressible vortex reconnection. *J. Fluid Mech.* **304**, 47–86.
WALEFFE, F. 1992 The nature of triad interactions in homogeneous turbulence. *Phys. Fluids* A **4** (2), 350–363.
WALEFFE, F. 1993 Inertial transfers in the helical decomposition. *Phys. Fluids* A **5** (3), 677–685.

https://doi.org/10.1017/jfm.2021.580 Published online by Cambridge University Press

WU, J.Z., MA, H.Y. & ZHOU, M.D. 2007 *Vorticity and Vortex Dynamics*. Springer Science & Business Media.

XIONG, S. & YANG, Y. 2019 Construction of knotted vortex tubes with the writhe-dependent helicity. *Phys. Fluids* **31** (4), 047101.

XIONG, S. & YANG, Y. 2020 Effects of twist on the evolution of knotted magnetic flux tubes. *J. Fluid Mech.* **895**, A28.

YAO, J. & HUSSAIN, F. 2018 Toward vortex identification based on local pressure-minimum criterion in compressible and variable density flows. *J. Fluid Mech.* **850**, 5–17.

YAO, J. & HUSSAIN, F. 2020*a* On singularity formation via viscous vortex reconnection. *J. Fluid Mech.* **888**, R2.

YAO, J. & HUSSAIN, F. 2020*b* A physical model of turbulence cascade via vortex reconnection sequence and avalanche. *J. Fluid Mech.* **883**, A51.

YAO, J. & HUSSAIN, F. 2020*c* Separation scaling for viscous vortex reconnection. *J. Fluid Mech.* **900**, R4.

YAO, J. & HUSSAIN, F. 2021 Polarized vortex reconnection. *J. Fluid Mech.* **922**, A19.

YU, Z., CHAPELIER, J.-B. & SCALO, C. 2018 Coherent-vorticity preserving large-eddy simulation of trefoil knotted vortices. In *2018 AIAA Aerospace Sciences Meeting*, p. 2090. The American Institute of Aeronautics and Astronautics.

ZHAO, X. & SCALO, C. 2019 Direct numerical simulation of trefoil knotted vortices. *APS* pp. Q12–003.

ZHAO, X., YU, Z., CHAPELIER, J.-B. & SCALO, C. 2021 Direct numerical and large-eddy simulation of trefoil knotted vortices. *J. Fluid Mech.* **910**, A31.

ZHAO, Y., YANG, Y. & CHEN, S. 2016 Vortex reconnection in the late transition in channel flow. *J. Fluid Mech.* **802**, R4.

ZUCCHER, S., CALIARI, M., BAGGALEY, A.W. & BARENGHI, C.F. 2012 Quantum vortex reconnections. *Phys. Fluids* **24** (12), 125108.

https://doi.org/10.1017/jfm.2021.580 Published online by Cambridge University Press